BNL-229061-2025-JAAM

Structure-Activity Relationships for Ethanol Dehydrogenation to Acetaldehyde by Silica-Supported Zinc Oxide Catalysts

B. Moskowitz, A. Frenkel

To be published in "ACS Catalysis"

October 2025

Chemistry Department

Brookhaven National Laboratory

U.S. Department of Energy

USDOE Office of Science (SC), Basic Energy Sciences (BES). Scientific User Facilities (SUF)

DISCLAIMER

ACS Catalysis

pubs.acs.org/acscatalysis
Research Article

Structure–Activity Relationships for Ethanol Dehydrogenation to Acetaldehyde by Silica-Supported Zinc Oxide Catalysts

Benjamin M. Moskowitz, Jisue Moon, Yuanyuan Li, Yongqiang Cheng, Luke L. Daemen, Lane Lee, Victor Fung, Aditya Savara, Anatoly I. Frenkel, Zili Wu, and Israel E. Wachs*

Cite This: ACS Catal. 2025, 15, 17225–17240
Read Online

ACCESS | Metrics & More | Article Recommendations | Supporting Information

ABSTRACT: Silica-supported ZnO efficiently catalyzes the nonoxidative dehydrogenation of ethanol to acetaldehyde, which is relevant for production of 1,3-butadiene from bioethanol. Characterization with *in situ* spectroscopies under dehydrated conditions (high sensitivity-low energy ion scattering (HS-LEIS), diffuse reflectance (DR) UV–vis, X-ray absorption spectroscopy (XAS), diffuse reflectance Fourier transform infrared spectroscopy (DRIFTS), inelastic neutron scattering (INS), and UV Raman), and ammonia adsorption probed by temperature-programmed desorption followed by DRIFTS and mass spectrometry (DRIFTS-MS NH_3-TPD), and DFT calculations revealed that the supported ZnO_x phase was present as isolated surface ZnO_x sites on SiO_2, with the vast majority coordinated by two siloxane bonds and one silicon atom with two nonbridging oxygens ($(\equiv SiO)_2Zn^{2+}O_2Si=$), anchored at 4-, 5-, and 6-membered siloxane rings. A minor fraction of surface ZnO_x sites possessed Lewis acidity, and even fewer sites possessed a Brønsted acidic $Zn(OH)^+Si$ moiety. Ethanol temperature-programmed surface reaction-mass spectrometry (TPSR-MS) with various oxidative or ethanol reaction pretreatments indicated that only sites with Lewis and Brønsted acidic character ($Zn(OH)^+Si$) were active for ethanol dehydrogenation, while the majority surface ($(\equiv SiO)_2Zn^{2+}O_2Si=$ sites were inactive. Greater heterogeneity among all surface ZnO_x sites, as assessed by *in situ* DR UV–vis spectroscopy, was associated with a greater number of ZnO_x sites that were active for ethanol dehydrogenation as well as lower enthalpic barriers for acetaldehyde production among the most active surface ZnO_x sites. Turnover frequencies and the apparent activation energy for ethanol dehydrogenation were determined from steady-state kinetics. Together, these findings suggested that anchoring inactive surface $(\equiv SiO)_2Zn^{2+}O_2Si=$ sites on the silica support caused a greater number of active surface ZnO_x sites to adopt a more strained configuration, promoting ethanol dehydrogenation catalysis. Pretreatments and catalysts that promoted desorption of ethanol during TPSR, taken as a marker of surface dehydroxylation, were associated with an increased number of the most active surface ($Zn(OH)^+Si$) sites. Such findings suggested that inactive surface ZnO_x sites were activated for ethanol dehydrogenation by dehydroxylation of the support and/or decreased coordination to hemilabile siloxane ligands.

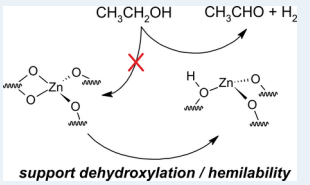

KEYWORDS: *SiO_2-supported, zinc oxide, ethanol dehydrogenation, acetaldehyde, active sites, kinetics, sampling technique, optical path length*

1. INTRODUCTION

Acetaldehyde is a key intermediate during the conversion of ethanol to 1,3-butadiene (BD).[1,2] In the two-step Ostromislensky process, nonoxidative dehydrogenation of ethanol to acetaldehyde is performed in an upstream reactor to feed an ethanol–acetaldehyde mixture to the BD synthesis reactor.[1,2] In the Lebedev process, ethanol conversion to BD proceeds in a single reactor, which is attractive in terms of process intensification and synergistic effects achieved in catalytic performance.[1,2] Ethanol dehydrogenation is recognized as the first step in the reaction pathway in the Lebedev process that is conducted with group 3–5 catalysts (catalysts featuring group 3 to 5 metal oxide domains, e.g., YO_x, HfO_x, ZrO_x, NbO_x, and TaO_x) that are supported on siliceous carriers or incorporated into siliceous zeolitic hosts as well as supported MgO/SiO_2 and bulk mixed oxide $MgO\text{-}SiO_2$ catalysts.[1,3−5] While group 3–5 catalysts and $MgO\text{-}SiO_2$ catalysts are efficient for C–C coupling toward BD, they exhibit poor ethanol dehydrogenation activity.[1,6] Therefore, promoters (e.g., Ag, Cu, and ZnO_x) that are efficient for nonoxidative ethanol dehydrogenation are added to the group 3–5 and $MgO\text{-}SiO_2$ catalysts for the Lebedev process.[1] The ZnO_x promoter has attracted particular attention because of observed[7] or proposed[8] synergistic effects that enhance BD production.

Ohira et al. proposed that ethanol molecularly adsorbs at ZnO_x sites with concerted O–H and α-C–H cleavage constituting the rate-determining step from temperature-programmed reaction studies under continuous ethanol flow over supported ZnO/SiO_2.[9] Qi et al. proposed that ethanol

Received: May 22, 2025
Revised: September 22, 2025
Accepted: September 23, 2025

https://doi.org/10.1021/acscatal.5c03430
ACS Catal. 2025, 15, 17225–17240

dehydrogenation over ZnO_x sites within a dealuminated Beta zeolite host (Zn-deAlBEA) proceeds via dissociative adsorption of ethanol to yield ethoxy coordinated to Zn and a Zn(OH)Si hydroxyl based on steady-state kinetic studies.[10] Hydrogen abstraction from the α-C of surface ethoxy to the hydrogen atom of the Zn(OH)Si moiety was also proposed to be the rate-determining step.[10] Yan et al. observed both molecularly adsorbed ethanol and surface ethoxy species over Zn-BEA at 350 °C with *in situ* DRIFTS, as well as their interaction with surface hydroxyl groups.[11] Acetaldehyde formation was observed at short times on stream, with subsequent formation of acetate and coupling products.[11]

Structure−activity relationships for supported ZnO_x promoters are typically lacking.[1] Wet kneading of ZnO nanoparticles with ZrO_2−SiO_2 yielded crystalline ZnO nanoparticles on the composite ZnO/ZrO_2−SiO_2 catalyst, while impregnation with zinc acetate dihydrate resulted in an amorphous material as indicated by XRD.[12] The initial acetaldehyde formation rates at 593 K from an ethanol−water mixture, however, were similar.[12] From a combination of DR UV−vis, DRIFTS, and XAS measurements, Chouillet et al. found that the ZnO_x component on supported ZnO/SiO_2 synthesized from incipient-wetness impregnation (IWI) of zinc nitrate hexahydrate was present as a poorly crystallized hemimorphite phase under hydrated conditions,[13] as corroborated by Taifan et al.[14] By contrast, IWI of zinc chloride yielded isolated $(SiO)_2Zn(O)Cl$ sites (where (O) indicated OH or H_2O) under *ex situ* (RT ambient) conditions according to EXAFS modeling.[15] Kunkel et al. determined that ZnO_x sites were highly dispersed and assigned as isolated ZnO_3 sites under dehydrated conditions for (VO_x)/ZnO_y-SiO_2 catalysts synthesized by a hydrothermal route according to *ex situ* and *in situ* UV−vis, Raman, and XANES spectroscopies.[16] Schweitzer et al. found that strong electrostatic adsorption synthesis of ZnO/SiO_2 yielded exclusively isolated ZnO_3 surface sites anchored at three-membered siloxane rings, as indicated by *in situ* XAS and UV Raman spectroscopy under dehydrated conditions (300−550 °C in He).[17] Such dehydrated conditions are more relevant to reaction conditions owing to the altered local coordination with the desorption of water.[17] Atomic layer deposition (ALD) with diethyl zinc onto SiO_2 also yielded isolated ZnO_3 sites.[18] The ZnO_x sites in Zn-BEA were observed as isolated $Zn^{2+}O_4$ sites under dehydrated conditions by *in situ* X-ray absorption spectroscopy (XAS).[10,19,20] Combining *in situ* FTIR and XAS characterization with steady-state kinetics, Qi et al. proposed that the active site for ethanol dehydrogenation was the $(SiO)_2(SiOH)_2Zn$ surface site featuring two covalent siloxane bonds and two silanol species donating their oxygen ligands.[10] However, the number of active sites was not quantified nor was direct evidence of silanols present within the inner coordination sphere of the Zn center (as opposed to, e.g., siloxane bridges) provided.

In this study, the molecular structures of surface ZnO_x sites present on supported ZnO/SiO_2 catalysts under dehydrated and ethanol dehydrogenation reaction conditions were elucidated by application of *in situ* high sensitivity-low energy ion scattering (HS-LEIS), DR UV−vis (diffuse reflectance ultraviolet−visible), DRIFTS (diffuse reflectance infrared Fourier transform), UV Raman, inelastic neutron scattering (INS), and XAS spectroscopic methods and DFT calculations. These complementary methods provide information on the composition of the outermost atomic layers (HS-LEIS), electronic structure (DR UV−vis and XANES), molecular and solid-state vibrations (DRIFTS, UV Raman, and INS), local atomic structure (EXAFS), and surface acidity (DRIFTS and DFT) that enabled the identification of diverse ZnO_x sites. Acetaldehyde yields obtained during CH_3CH_2OH-TPSR-MS indicated that most of the surface ZnO_x sites present as $(\equiv SiO)_2ZnO_2Si=$ sites were inactive. Rather, isolated surface ZnO_x sites with both Lewis and Brønsted acidic character constitute the catalytic active site for ethanol dehydrogenation. The Brønsted acid site was revealed to be a $Zn(OH)^+Si\equiv$ moiety. Two distributions of the surface ZnO_x active sites were identified with higher and lower enthalpic barriers for acetaldehyde production. Through correlation with characterization by *in situ* DR UV−vis spectroscopy, it was found that greater heterogeneity among all surface ZnO_x sites (e.g., more diverse local molecular geometries) was associated with lower enthalpic barriers for acetaldehyde production among the most active surface ZnO_x sites. Additionally, dehydroxylation of the surface, as indicated by the desorption of ethanol during TPSR as a probe of labile siloxane bonds,[21] was associated with increasing the number of the most active surface ZnO_x sites. Together, these findings suggest that strain is a key catalytic activity descriptor for surface ZnO_x sites on SiO_2.

2. METHODS

2.1. Catalyst Synthesis. *2.1.1. Support Preparation.* Fumed silica (Cab-O-Sil EH-5, Cabot) was dispersed in deionized (DI) water (18.2 MΩ, Milli-Q), dried at 120 °C in static air for 48 h in a muffle furnace (Thermolyne 48000), crushed with an agate mortar and pestle, and sieved to retain 250−425 μm aggregates. The silica was then calcined in the muffle furnace at 500 °C for 4 h (ramp rate 1 °C min^{-1}) in 100 cm^3 min^{-1} flowing dry air (Airgas AI D300).

2.1.2. Incipient-Wetness Impregnation. In an exemplary synthesis, 2% ZnO loading was achieved by dissolving 0.12 g of zinc acetate dihydrate (98.0−101.0%, Alfa Aesar) in 1.91 g of DI water (18.2 MΩ, Milli-Q) (wetness point of 0.9 mL g^{-1}). The zinc acetate solution was added dropwise to 2.15 g of the silica support while stirring. The impregnated silica was further stirred for 30 min and dried in ambient air at 25 °C for 16 h. The catalyst was calcined in the muffle furnace at 500 °C for 4 h (ramp rate 5 °C min^{-1}) in 100 cm^3 min^{-1} flowing dry air. The weight of impregnated zinc acetate dihydrate was varied to achieve various ZnO loadings. These catalysts are designated by the code "IWI."

2.1.3. Strong Electrostatic Adsorption (SEA). The catalyst synthesis methodology of Schweitzer et al. was adapted.[17] Initially, 18.00 g of the silica support particles was suspended in 150 mL of DI water (18.2 MΩ, Milli-Q) in a 500 mL high-density polyethylene (HDPE) bottle. Over the course of ∼1 h, the pH of the solution was adjusted to 11.3 by adding 164 mL of an ammonium hydroxide solution (Acros Organics, 28−30 wt %). In a separate HDPE bottle, 3.80 g of zinc nitrate hexahydrate (98%, Sigma-Aldrich) was dissolved in DI water and adjusted to pH 11.3 using 56 mL of the ammonium hydroxide solution. A white precipitate was initially observed, but adjustment above pH 10 with ammonium hydroxide resulted in a clear, colorless solution. The basic zinc solution was rapidly added to the silica suspension, and the resulting suspension was shaken on an orbital shaker (Glas-Col 099A PVM12) for 10 min. The suspension was allowed to settle for 5 min, and then the solution was decanted. The resultant slurry was rinsed with 150 mL of DI water and shaken on the orbital

https://doi.org/10.1021/acscatal.5c03430
ACS Catal. 2025, 15, 17225−17240

shaker for 10 min, vacuum-filtered, rinsed several times with DI water, dried overnight in static air at 125 °C in a drying oven, and then calcined in a muffle furnace (Lindberg/Blue, Thermo Scientific) at 500 °C for 4 h (ramp rate 1 °C min^{-1}) in flowing dry air (Ultra Zero, Airgas). This catalyst is designated by the code "SEA." The ZnO loading for the ZnO/SiO_2-SEA sample was determined to be 3.7 ± 0.3% using X-ray absorption spectroscopy (*vide infra*). Additionally, the SiO_2 support was subjected to the same ammonium hydroxide treatment without addition of any zinc solution and dried and calcined in the same way (designated by the code "NH_4OH").

2.2. Additional Methods. Additional methods are described in the Supporting Information (Section S1).

3. RESULTS

3.1. N_2 Physisorption and Powder XRD. Compared to the parent silica support, the supported 3.7% ZnO/SiO_2-SEA sample lost considerable mesoporosity, surface area, and pore volume, which was attributed to Ostwald ripening[22] during synthesis (these results are discussed in detail in Section S2.1). In contrast, the SiO_2-NH_4OH sample did not lose as much mesoporosity, surface area, and pore volume. Clearly, the silica dissolution kinetics and exposure time dictated the resultant morphological changes. These textural impacts on the ZnO/SiO_2-SEA sample contrast with a previous report[17] and suggest significant modifications to the silica by the SEA synthesis herein (see Section 3.4). The XRD characterization of the bulk ZnO sample is discussed in Section S2.2 and confirms its hexagonal wurtzite crystal structure.

3.2. *In Situ* and *Ex Situ* HS-LEIS. The *in situ* depth profile of the surface composition of the dehydrated supported 2% ZnO/SiO_2-IWI catalyst (Figure S4A) shows that the Zn signal nearly completely diminishes within ∼0.6 nm, a distance that corresponds to one to two atomic layers. This result indicates that the supported ZnO_x phase is two-dimensionally dispersed on the silica support under dehydrated conditions. The corresponding *ex situ* integrated Zn signal intensity of the outermost atomic layer is plotted as a function of Zn surface density in Figure S4B. The results are well described by a linear fit that is zero-crossing within experimental error. Such behavior is consistent with two-dimensionally dispersed surface ZnO_x sites on the SiO_2 support. HS-LEIS is a line-of-sight technique; hence, it is assumed that the external surface of the aggregates is representative of that within the pores. The slightly lower absolute intensity observed under *ex situ* conditions compared to *in situ* conditions may be attributed to adsorbed water on the catalyst surface remaining after evacuation and partial clustering of the supported ZnO_x phase on SiO_2 in the presence of adsorbed moisture. Altogether, HS-LEIS revealed that the supported ZnO_x phase is essentially present as two-dimensionally dispersed surface ZnO_x sites.

3.3. *In Situ* DRIFTS under Dehydrated Conditions. *In situ* DRIFTS spectra of silica-supported ZnO catalysts were obtained under dehydrated conditions to probe the anchoring of ZnO_x species to the silica support (Figure S5). In the hydroxyl region (Figure S5A), the intensities at 3742 cm^{-1} (assigned to terminal, free silanols)[23] and at 3680 and 3560 cm^{-1} (both assigned to hydrogen-bonded vicinal silanols)[23] slightly decrease with increasing ZnO_x loading for the supported ZnO/SiO_2-IWI catalysts, which is attributed to the anchoring of ZnO_x species at surface hydroxyls on the silica support. The SiO_2-NH_4OH support and the supported ZnO/SiO_2-SEA catalyst both exhibit increase at 3680 and 3560 cm^{-1} from H-bonded vicinal silanol hydroxyls, attributed to Ostwald ripening during synthesis.[22] Compared to the SiO_2-NH_4OH support, the supported 3.7% ZnO/SiO_2-SEA catalyst exhibits a decrease in the band at 3742 cm^{-1} from terminal, free silanols. By subtracting the spectrum of the SiO_2 support from that of ZnO/SiO_2-IWI catalysts and of SiO_2-NH_4OH from that of 3.7% ZnO/SiO_2-SEA (Figure S5B), it is revealed that terminal, free silanol consumption is centered at 3745 cm^{-1}, which is consistent with isolated silanols, rather than geminal or vicinal silanols.[24]

In the skeletal region (Figure S5C), the bands at 825, 978, and 1085 cm^{-1} are assigned to the $\nu_s(Si{-}O{-}Si)_{TO/LO}$, $\nu(Si{-}OH)$, and $\nu_{as}(Si{-}O{-}Si)_{TO}$ modes of the silica support, respectively, where TO indicates transverse optical and LO indicates longitudinal optical.[17,25] All silica-supported ZnO samples exhibit an increase at 930 cm^{-1} assigned to $\nu_s(Zn{-}O{-}Si)$[26,27] relative to $\nu_s(Si{-}O{-}Si)_{TO/LO}$ mode; the latter may be considered to a first approximation as an internal standard for the bulk SiO_2 lattice. The intensities of the $\nu_s(Zn{-}O{-}Si)$ and $\nu(Si{-}OH)$ modes increased and decreased, respectively, with increasing surface ZnO_x density, which is attributed to anchoring of surface ZnO_x sites at surface silanols. Altogether, *in situ* DRIFTS revealed that ZnO_x species anchored at terminal, free silanols to form Zn−O−Si bonds

The impact of the mesh "chair", used to support the samples, on the DRIFTS spectra of the SiO_2 support are discussed in Section S2.3.1.

3.4. *In Situ* UV Raman Spectroscopy under Dehydrated Conditions. Silica-supported ZnO catalysts were probed under dehydrated conditions by *in situ* UV Raman spectroscopy to further understand the anchoring of ZnO_x species to the silica support. *In situ* UV Raman spectra (244 nm excitation) of supported ZnO/SiO_2−IWI and SiO_2 are shown in Figure 1A. Assignments for the band determined from the deconvolution analysis are summarized in Table S4. For clarity, the nomenclature for the band at 957 cm^{-1} assigned to $\nu(Si{-}O)_{Q2}$ indicates Q^2 SiO_4 with two Si−O−Si bonds and two so-called nonbridging oxygens (e.g., oxygens that constitute silanols (Scheme 1A) or ionically bonded with cations (Scheme 1B)).[28−30]

The evolution of normalized Raman band areas with ZnO loading is presented in Figure 1B, where normalization was performed with respect to the $\nu_s(Si{-}O{-}Si)_{TO/LO}$ mode at 808−814 cm^{-1} (Section S1.5). The band area for Q^2 species is linear with respect to ZnO_x loading, indicating that Q^2 species provide anionic coordinating oxygens to Zn cations that modify the glass network (and form Zn−O−Si bonds, Scheme 1B), as opposed to forming covalent bonds as part of the glass network.[30,31] The linear increase of the Zn−O−Si bonds indicates that the ZnO_x domains are two-dimensionally dispersed on the silica support, consistent with *in situ* DRIFTS and *in situ* HS-LEIS. The band area of the three-membered siloxane rings (3MR) at 611 cm^{-1} decreases 53 ± 2% for the 2% ZnO/SiO_2-IWI sample compared to the silica support. This indicates that some portion of ZnO_x sites anchor at 3MR on the silica surface.[17,32] For the supported 7% ZnO/SiO_2-IWI sample, the 3MR band area is within experimental error of the silica support. The nonlinear trend of the $\nu(Si{-}O{-}Si)_{3MR}$ band area suggests that ZnO_x is not preferentially anchoring at the Si−O−Si 3MR site. Altogether, *in situ* Raman spectroscopy with 244 nm excitation indicates that the ZnO_x sites are two-dimensionally dispersed on the silica support and anchored via ionic bonds.

https://doi.org/10.1021/acscatal.5c03430
ACS Catal. 2025, 15, 17225−17240

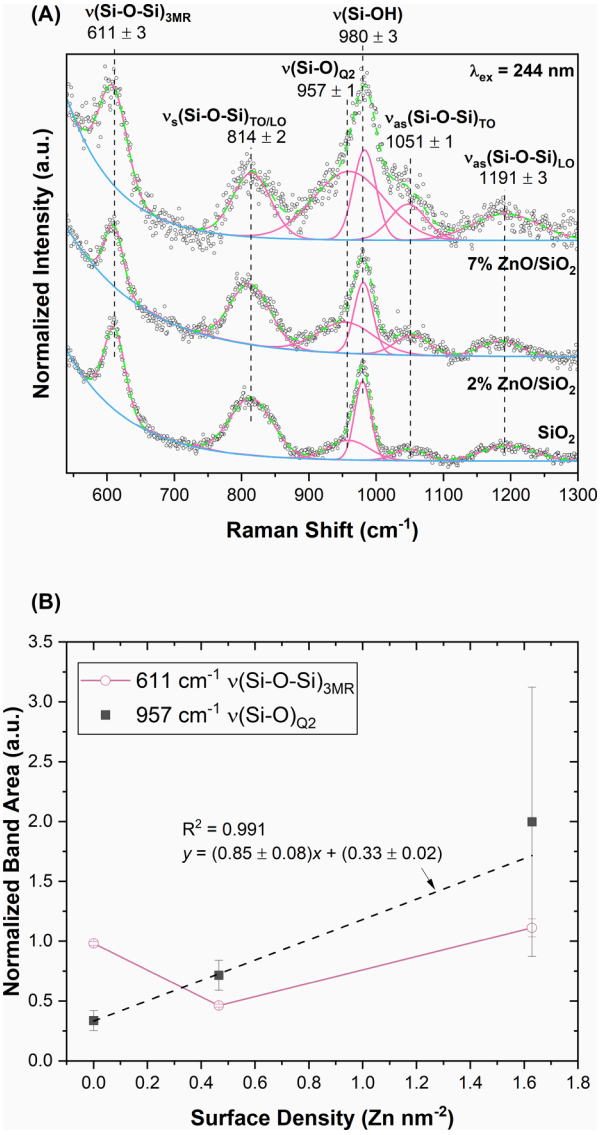

Figure 1. (A) *In situ* UV Raman spectra (244 nm excitation) of SiO_2, supported 2% ZnO/SiO_2–IWI, and supported 7% ZnO/SiO_2–IWI under dehydrated conditions at 120 °C in 1.25% O_2/24% He/Ar following treatment at 400 °C in the same gas mixture. Black circles: Raman spectrum, blue line: baseline, pink line: fitted Gaussian bands, green line: cumulative spectral fit. (B) Normalized band areas for $\nu(Si{-}O{-}Si)_{3MR}$ (open circle) and $\nu(Si{-}O)_{Q2}$ (filled square) from deconvolution analysis in (A) as a function of surface Zn density. Dashed black line: linear fit for $\nu(Si{-}O)_{Q2}$.

Scheme 1. Q^2 Silicon Atoms that Feature Two Si–O–Si Bonds and Two Nonbridging Oxygens that Are Bonded to (A) Hydrogen Atoms (i.e., Forming Silanol Groups) and (B) a Zn Cation[a]

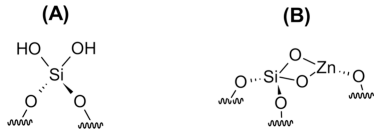

[a]Wavy lines indicate silicon atoms of the silica support.

The SiO_2, SiO_2-NH_4OH, and supported 3.7% ZnO/SiO_2-SEA samples were also examined with *in situ* UV Raman spectroscopy with 325 nm excitation (Figure S7A). Deconvolution analysis (Figure S7B) shows that the SiO_2-NH_4OH sample exhibits an increase in 3MR and a decrease in silanols relative to SiO_2, indicating that the extended NH_4OH treatment condensed silanols to form three-membered siloxane rings. The supported 3.7% ZnO/SiO_2-SEA sample exhibits a decrease in the quantity of three-membered siloxane rings compared to SiO_2-NH_4OH, suggesting that ZnO_x species anchor at 3MR. The Raman spectrum of supported 3.7% ZnO/SiO_2-SEA also confirms the absence of crystalline ZnO nanoparticles,[33,34] hemimorphite ($Zn_4(Si_2O_7)(OH)_2{\cdot}H_2O$),[35] willemite ($Zn_2SiO_4$),[36] clinopyroxene ($ZnSiO_3$),[37] and ilmenite ($ZnSiO_3$).[37] The absence of a band at 957 cm^{-1} for Q^2 species for all 325 nm excited samples (including the same SiO_2 sample) suggests resonance Raman enhancement for this species when excited with 244 nm excitation. Altogether, Raman spectroscopy with 325 nm excitation indicates that the ZnO_x species are two-dimensionally dispersed for the supported 3.7% ZnO/SiO_2-SEA sample and that a portion of ZnO_x species anchor at three-membered siloxane rings.

The same *in situ* Raman spectra above were replotted with extended spectral range (Figure S8). Bands are observed at ~440 cm^{-1} (the so-called R-band[38]) and ~490 cm^{-1} (the so-called D_2 band[39]) that have been assigned to the vibrations of 5/6-membered $(SiO)_x$ rings in the silica network and to four-membered siloxane rings, respectively.[17,39,40] The SiO_2-NH_4OH sample exhibited an increase in the R-band and the D_2 band compared to the SiO_2 support. Thus, silanols were also condensed to form 4-, 5-, and 6-membered rings on the SiO_2 surface following NH_4OH treatment. Furthermore, the R-band and the D_2 band increased with Zn loading for both IWI (Figure S8A) and SEA (Figure S8B) samples. These results indicate that ZnO_x species anchored to create new 4-, 5-, and 6-membered $(SiO)_x$ rings. Altogether, it may be concluded that while ZnO_x species may anchor at 3MR or elsewhere on the silica support, they also form larger (4-/5-/6-membered) metallacyclic rings upon anchoring, reflecting the dynamic nature of the SiO_2 surface.[41]

3.5. *In Situ* DR UV–vis Spectroscopy under Dehydrated Conditions. Silica-supported ZnO catalysts were probed with *in situ* DR UV–vis spectroscopy to understand the electronic structure of ZnO_x sites and the implications for molecular structure. The *in situ* DR UV–vis spectrum of the silica support under dehydrated conditions (Figure S9A) showed weak absorption at 39 090 ± 30 cm^{-1} (fwhm 6200 ± 100 cm^{-1}) assigned to the B_2 band of an oxygen-deficient center, whose probable structure is a twofold coordinated silicon atom (i.e., a silylene, =Si:), and at 48 990 ± 30 cm^{-1} (fwhm 4990 ± 80 cm^{-1}) assigned to an oxygen-deficient E' center, with one SiO_3 unit relaxed to a planar or puckered configuration.[42] *In situ* DR UV–vis spectra of the supported ZnO/SiO_2-IWI and ZnO/SiO_2-SEA catalysts under dehydrated conditions (Figure S9A) exhibited an absorption edge starting at ~40 000 to 45 000 cm^{-1} that is assigned to an $O^{2-} \rightarrow Zn^{2+}$ ligand-to-metal-charge-transfer (LMCT) band of dispersed ZnO_x surface sites.[13,43] By contrast, bulk ZnO exhibits an absorption edge starting at ~25 000 cm^{-1} attributed to the direct band gap of the bulk phase.[44] The supported 1% ZnO/SiO_2-IWI catalyst exhibits a weak band at 38 880 ± 70 cm^{-1} (fwhm 5400 ± 200 cm^{-1}) assigned to the B_2 band of an oxygen-deficient center of the silica support[42,45] as well as a weak, broad absorption at <30 000 cm^{-1} attributed to regular reflection from a slightly larger agglomerate size fraction.

https://doi.org/10.1021/acscatal.5c03430
ACS Catal. 2025, 15, 17225–17240

The edge position was quantitatively assessed via the edge energy (E_g) values reported in Figure S9B. The edge energies of the supported ZnO/SiO_2-IWI catalysts are constant with respect to Zn surface density at 5.9 ± 0.1 eV. The edge energy of the supported 3.7% ZnO/SiO_2-SEA catalyst is 6.1 ± 0.1 eV and falls within the confidence interval of the ZnO/SiO_2 data (p-value, p = 0.05).[46] Consequently, a linear fit among the supported ZnO/SiO_2-IWI and 3.7% ZnO/SiO_2-SEA samples exhibits a slope not statistically different than zero (p = 0.37). By contrast, the crystalline ZnO reference material exhibits a much smaller direct band gap at 3.2 ± 0.1 eV, consistent with literature reports for bulk ZnO.[44] These results are consistent with the absence of a significant concentration of ZnO nanoparticles on the silica-supported catalysts. Furthermore, there is no evidence for the presence of crystalline nanoparticles of α-Zn_2SiO_4 (direct E_g = 5.1 eV),[47] β-Zn_2SiO_4 (direct E_g = 4.0 eV),[48] $ZnSiO_3$ (direct E_g = 2.9 eV), nor $Zn_4Si_2O_7(OH)_2$ (direct E_g calculated herein as 5.5 eV)[49,50] phases on the silica-supported ZnO catalysts. The *in situ* UV−vis results for the silica-supported ZnO catalysts are, thus, consistent with a two-dimensionally dispersed surface ZnO_x phase. Furthermore, the constant direct band gap for the supported ZnO/SiO_2 catalysts with respect to surface Zn density indicates that the surface ZnO_x domain size is invariant with surface ZnO_x coverage.[51]

The peak parameters associated with the Zn^{2+} LMCT band were assessed by fitting (Figure S9C and Table S5). The Zn^{2+} LMCT band is linear with respect to ZnO loading for the supported ZnO/SiO_2-IWI and 3.7% ZnO/SiO_2-SEA catalysts (Figure S9D), indicating that the resulting ZnO_x sites are two-dimensionally dispersed for both synthesis methods. The ZnO loading for the supported 3.7% ZnO/SiO_2-SEA catalyst, as indicated by its Zn^{2+} LMCT band area, is consistent with that quantitatively determined by XAS. The Zn^{2+} LMCT band had very similar fitted maxima for the supported ZnO/SiO_2-IWI and ZnO/SiO_2-SEA catalysts at 52 100−54 500 cm^{-1} (6.99−7.31 eV, Table S5). Such a peak position is consistent with isolated Zn_1O_4 sites rather than isolated Zn_1O_3 sites according to TD-DFT calculations by Kunkel et al.[16] The broadness of the band, however, indicated by the full width at half-maximum (fwhm), generally increased with increasing ZnO loading (Table S5). This increased broadness suggests an increasing heterogeneity of ZnO_x structures.[52] In summary, *in situ* DR UV−vis spectroscopy confirmed the two-dimensionally dispersed nature of surface ZnO_x sites, indicated isolated Zn_1O_4 sites, and suggested a greater heterogeneity in their electronic structures with increasing surface ZnO_x coverage.

3.6. *In Situ* INS Spectroscopy. Silica-supported ZnO catalysts were probed with *in situ* INS spectroscopy to reveal the vibrational modes of H-containing species. The simulated INS spectrum of bulk ZnO agrees well with the experimental *in situ* INS spectrum as shown in Figure S10. This result validates the theoretical INS simulation approach employed herein. The *in situ* INS spectra of supported 3.7% ZnO/SiO_2-SEA, SiO_2-NH_4OH, and ZnO, as well as a spectrum of the SiO_2-R sample under ambient conditions are shown in Figure S11. The supported 3.7% ZnO/SiO_2-SEA sample exhibits scattering at 765 cm^{-1} that was not observed in the SiO_2-NH_4OH, SiO_2-R, or ZnO samples. To understand the origin of this band, simulations of the atom-projected INS spectra of hydroxyl and hydride H atoms present in cluster DFT models of SiO_2 and supported ZnO_x/SiO_2 with isolated ZnO_x species (Figure S12) were undertaken. The results of these simulations (Figure S13 and Table S6) suggest that a bridging $Zn(OH)^+Si$ hydroxyl hydrogen-bonded through its H atom may be consistent with the 765 cm^{-1} vibrational mode.

The discrepancy between the simulated H-bonded $Zn(OH)^+Si$ modes (642−709 cm^{-1}) and the experimental 765 cm^{-1} mode might be attributed to the simplified cluster structural models used rather than anharmonic effects. INS simulations were conducted under the harmonic approximation.[53] While anharmonicity is expected for this H-bonded mode, this effect alone is expected to result in an experimental mode red-shifted relative to the theoretical mode.[54]

3.7. *In Situ* XAS under Dehydrated and Reaction Conditions. Under ambient, dehydrated, and ethanol reaction conditions, *in situ* X-ray absorption near edge structure (XANES) spectra indicated that the silica-supported ZnO_x sites possessed Zn^{2+} cations in the ZnO_4 coordination environment (Figure S14B−D and Table S7). The supported 2% ZnO/SiO_2-IWI, 7% ZnO/SiO_2-IWI, and 3.7% ZnO/SiO_2-SEA catalysts were probed by *in situ* XAS, with the 3.7% ZnO/SiO_2-SEA sample studied only under ambient and dehydrated conditions. The edge energy (E_0 energy) for Zn changes monotonically with its oxidation state, and the oxidation state of silica-supported ZnO samples was assigned by comparison to Zn foil (Zn^0) and zinc acetate dihydrate (Zn^{2+}) (Figure S14A and Table S7).[17] In addition, the absorption edge region in the XANES spectra for all supported ZnO/SiO_2 catalysts exhibit two peaks at 9665 and 9668−9669 eV assigned to ZnO_4 coordination[55] rather than two distinct ZnO_x sites.[56] It is further noted that the XANES spectra possessed a similar line shape as reported elsewhere for supported ZnO/SiO_2[13,14,57,58] and ZnO/SiO_2-SEA.[17]

In situ XANES further indicated that not all ZnO_x sites were coordinated by surface intermediates under ethanol reaction conditions. This finding may reflect that not all surface ZnO_x sites were active for ethanol dehydrogenation and/or a lower coverage of reactive surface intermediates at the reaction temperature (330 °C). Such assessments were made with a linear combination fitting (LCF) methodology (Figure S15 and Table S8). In the absorption edge region (Figure S14B−D), all supported ZnO/SiO_2 catalysts exhibited lower intensity under dehydrated conditions as compared to ambient conditions, which is attributed to lower first shell coordination number and/or greater local disorder.[55,59] During ethanol flow, the near edge intensity slightly increased and could be associated with adsorption of reaction intermediates during ethanol dehydrogenation at ZnO_x sites, with commensurate increased Zn inner sphere coordination and/or induced greater centrosymmetry.[60] The fraction of surface ZnO_x sites with greater coordination and/or centrosymmetry under ethanol reaction conditions was quantified for the supported 2 and 7% ZnO/SiO_2-IWI catalysts as 16 and 11%, respectively, by LCF (Figure S15 and Table S8). These results suggest that a greater fraction of ZnO_x sites interact with adsorbates for 2% ZnO/SiO_2-IWI as compared to 7% ZnO/SiO_2-IWI under the same reaction conditions, indicating a greater abundance of active sites for the former catalyst rather than a coverage effect. Although *in situ* XANES spectra obtained at different temperatures were used as LCF standards, the supported ZnO/SiO_2 samples at 400 °C in O_2/He could be ∼100% fit by the corresponding 330 °C in flowing He spectra, indicating minimal effect of temperature on the fitting process.

In situ extended X-ray absorption fine structure (EXAFS) analysis corroborated the conclusions reached from the

https://doi.org/10.1021/acscatal.5c03430
ACS Catal. 2025, 15, 17225−17240

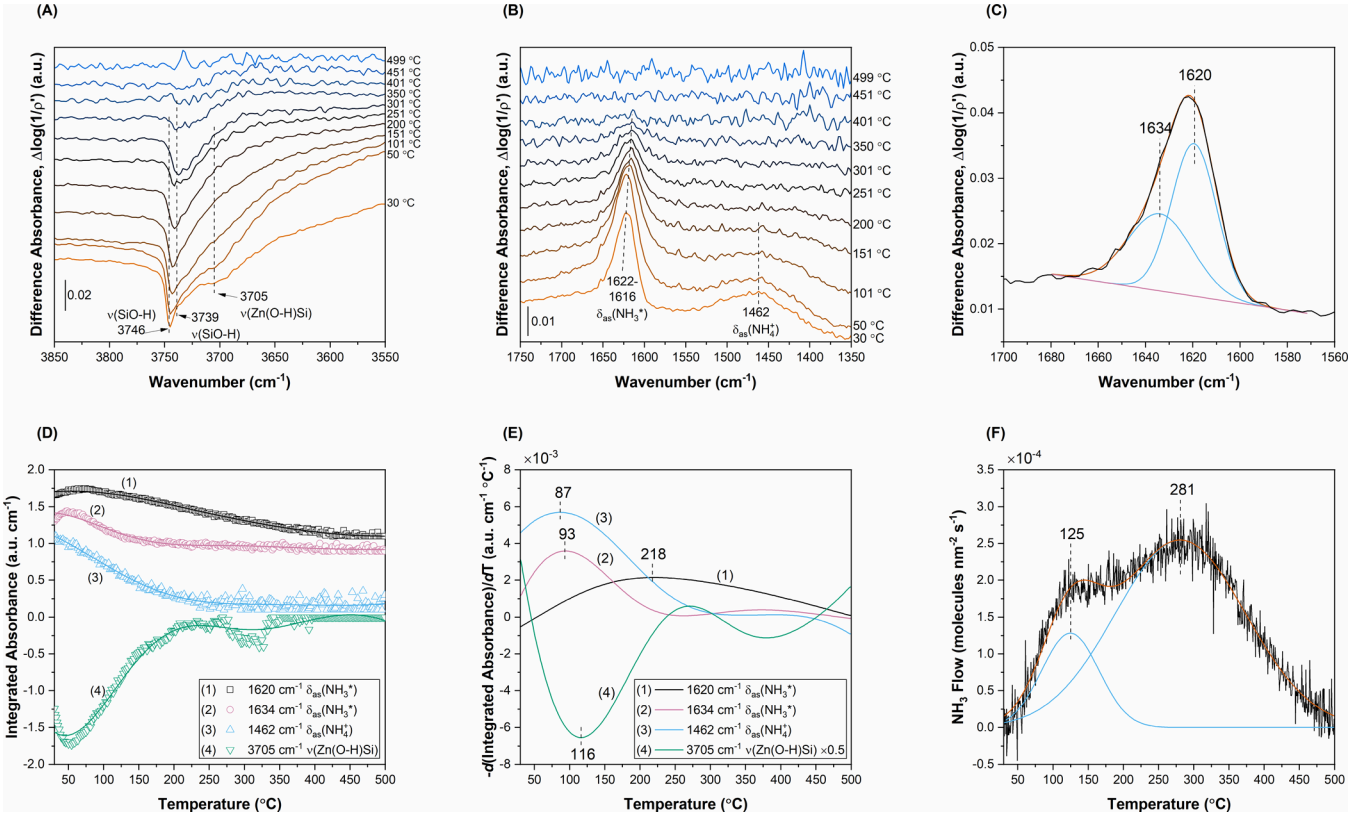

Figure 2. *In situ* DRIFTS-MS NH_3-TPD of supported 3.7% ZnO/SiO_2-SEA following NH_3 adsorption and flushing in Ar at 30 °C. (A) Selected difference IR spectra in hydroxyl stretching region. (B) Selected difference IR spectra in the NH_3 bending region. (C) Band at 1623 cm^{-1} at 30 °C (black), deconvolution with Gaussian peaks (blue), cumulative fit (red), and baseline (pink). (D) Integrated IR absorbance versus temperature (symbols) and smoothed results (solid lines). Symbols and lines enumerated (1), (2), (3), and (4) are offset by 1.1, 0.9, 0.1, and 0.0 au cm^{-1}, respectively. (E) Negative of the first derivative of smoothed, integrated absorbance with respect to temperature, which is proportional to the ammonia desorption rate. (F) NH_3 flow measured by MS (black), deconvolution with Gaussian peaks (blue), and cumulative fit (red).

corresponding XANES spectra regarding local coordination and coordination by surface intermediates under ethanol reaction conditions. Furthermore, *in situ* EXAFS revealed that the majority of surface ZnO_x sites were consistent with an isolated Zn_1O_4 structure. The *in situ* EXAFS spectra of supported 2% ZnO/SiO_2-IWI, 7% ZnO/SiO_2-IWI, and 3.7% ZnO/SiO_2-SEA catalysts appeared quite similar (Figure S16B–D) and are discussed in detail in Section S2.4.1. Inspection of the EXAFS spectra for the supported ZnO/SiO_2 catalysts suggested that Zn centers had four oxygen atoms in the first shell. For comparison, ZnO and zinc acetate dihydrate reference materials have four and six, respectively, oxygen atoms surrounding Zn. This first shell coordination slightly decreased upon dehydration from ambient conditions to 400 °C in O_2/He (Tables S10 and S12), which confirms the surface nature of the ZnO_x sites. The decrease observed for 7% ZnO/SiO_2 upon dehydration was not statistically significant (Table S11, $p = 0.18$). There appears to be fewer second shell neighbors for ZnO/SiO_2 as compared to ZnO, which is expected for highly dispersed sites.

The identity of the atoms in the first and second shells around the Zn absorber for ZnO/SiO_2 catalysts was examined qualitatively via the wavelet transform (WT) of the EXAFS spectra and is discussed in detail in Section S2.4.2. Altogether, WT analysis of supported ZnO/SiO_2 catalysts indicates that Zn_1O_x sites are isolated on the silica support under hydrated and dehydrated conditions with Si (and not Zn) in the second coordination shell.

The local atomic structure of the surface ZnO_x sites on ZnO/SiO_2 catalysts was quantitatively analyzed via fitting of the EXAFS spectra (Figures S21–S23 and Tables S10–S12). All catalysts possessed $ZnO_{4/5}$ coordination under ambient conditions. All catalysts, however, possessed ZnO_4 coordination under dehydrated and ethanol reaction conditions. This Zn local environment reflected the loss of coordinating water from ambient conditions. The first shell oxygen coordination number was consistent with analysis of the XANES region and visual inspection of the EXAFS spectra. Altogether, *in situ* EXAFS analysis indicated that the majority of ZnO_x sites were isolated Zn_1O_4 sites under dehydrated and reaction conditions.

3.8. *In Situ* DRIFTS-MS NH_3-TPD. The NH_3-TPD studies were performed with the supported 3.7% ZnO/SiO_2-SEA sample and simultaneously monitored with DRIFTS and MS to probe the catalyst surface acid sites. Interaction with ammonia resulted in three negative bands at 3746, 3739, and 3705 cm^{-1} (Figure 2A), which are assigned to the ν(SiO–H) vibrational mode of isolated terminal silanols,[23] the ν(SiO–H) vibrational mode of geminal or vicinal silanols,[24] and the ν(Zn(O–H)$^+$Si) vibrational mode of a bridging hydroxyl between zinc and silicon centers, respectively. The 3705 cm^{-1} band is not consistent with a terminal ZnOH hydroxyl, which was predicted to vibrate at 3571–3572 cm^{-1} according to DFT calculations of silica-supported isolated ZnO_x domains.[61] A positive band at 1622 cm^{-1} (Figure 2B) is assigned to the $\delta_{as}(NH_3^*)$ mode of ammonia adsorbed at Lewis acid sites.[62] The 1622 cm^{-1} band appears to shift to 1616 cm^{-1} with

https://doi.org/10.1021/acscatal.5c03430
ACS Catal. 2025, 15, 17225–17240

increasing temperature, and deconvolution analysis reveals two peaks present at 1634 and 1620 cm^{-1} (Figure 2C) that are assigned to two distinct Lewis acid sites (termed type α and β, respectively). The positive band at 1462 cm^{-1} (Figure 2B) is assigned to $\nu_{as}(NH_4^+)$ of ammonia adsorbed at Brønsted acid sites.[62]

The kinetic correspondence of the surface ammonia species during temperature-programmed desorption further confirmed the above assignments. Ammonia adsorbed at both Brønsted acid sites and the interaction of adsorbed ammonia with $Zn(OH)^+Si$ bridging hydroxyls fully diminished by ~250 °C (Figure 2D), confirming that $Zn(OH)^+Si$ bridging hydroxyls constitute Brønsted acid sites. Ammonia adsorbed at type α-Lewis acid sites decayed to zero coverage by ~175 °C, while ammonia adsorbed at type β-Lewis acid sites remained adsorbed until ~400 °C.

Ammonia desorbed from type α-Lewis acid sites and Brønsted acid sites and ceased to interact with $Zn(OH)^+Si$ hydroxyls with a T_p at ~100 °C, while type β-Lewis acid sites exhibited a T_p of 218 °C (Figure 2E). A fitting analysis of the desorption rate of ammonia measured in the gas phase by MS (Figure 2F) revealed two peaks. The desorption of ammonia into the gas phase with a T_p of 125 °C closely matches the T_p of both $Zn(OH)^+Si$ Brønsted acid sites and type α-Lewis acid sites. Desorption of ammonia into the gas phase with a T_p of 281 °C is more coincident with desorption of ammonia from type β-Lewis acid sites.

In situ DRIFTS-MS NH_3-TPD of 1% ZnO/SiO_2-IWI (Figure S24) resembles the results for 3.7% ZnO/SiO_2-SEA (Figure 2), while the SiO_2 support did not initially possess any Lewis nor Brønsted surface acidity (Section S2.5). Altogether, *in situ* DRIFTS-MS-NH_3-TPD revealed that weaker type α-Lewis acid-Brønsted acid $Zn(OH)^+Si$ pair sites and stronger type β-ZnO_x Lewis acid sites are present for supported ZnO/SiO_2 catalysts. The discrepancy in T_p values between IR and MS data is attributed to readsorption of gaseous NH_3 in the catalyst bed.

Furthermore, quantification of the MS-TPD results showed that total Lewis acid sites linearly increase with surface Zn densities while Brønsted acid sites are more predominant at a low surface Zn density (Figure 3 and Table S13). Together, this indicates that the weaker type α-Lewis acid-Brønsted acid $Zn(OH)^+Si$ pair sites are more predominate at lower Zn surface densities, while type β-Lewis acid sites predominate at higher surface densities.

3.9. DFT Calculations of NH_3 Adsorption. Cluster DFT calculations were performed to model ammonia adsorption on isolated ZnO_x sites featuring Zn_1O_4 coordination with a Q^2 silicon ligand ("Zn-4c"), Zn_1O_3 coordination ("Zn-catalyst"), and Zn_1O_4 coordination with a terminal ZnOH ligand ("Zn-3-OH") (Figure S26). Adsorption at zinc Lewis acid sites (Figure S26A–C) and putative Brønsted acid bridging hydroxyl sites (Figure S26D–F) were considered. The Zn-4c model exhibited weak binding of NH_3* at its Lewis acid site (Table S14), comparable to DFT calculations of NH_3 adsorption on cluster models of silica.[63] Adsorption of ammonia at the bridging hydroxyl of Zn-4c was of moderate strength, but Mulliken charge analysis revealed that no NH_4^+ species were formed. In fact, such binding was comparable to that calculated for an isolated silanol also present in the Zn-4c model. The Zn-catalyst model exhibited moderate and similar (within 0.1 eV) binding energies at its Lewis and Brønsted acid sites. The Zn-3-OH model exhibited a similar Lewis acid binding energy as

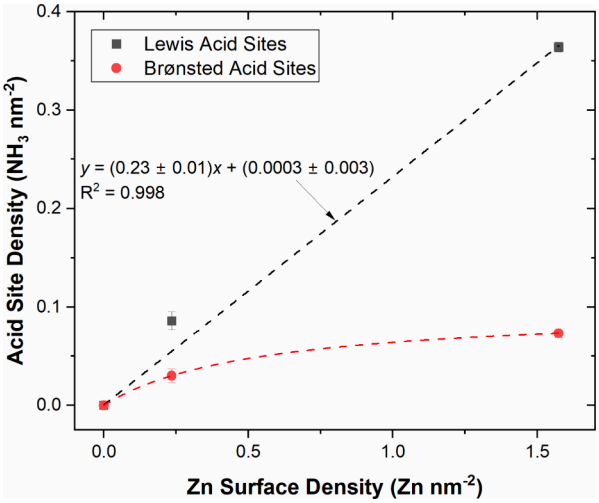

Figure 3. Lewis (square) and Brønsted (circle) acid site surface density as a function of surface Zn density. Dashed black line indicates linear regression of Lewis acid sites. Dashed red line indicates empirical model of the form $y = abx/(1 + bx)$, where x and y are the Zn and Brønsted acid site surface densities, respectively. Values for a and b were fitted as 0.10 and 1.9, respectively.

the Zn-catalyst model, but its Brønsted acid binding energy was weaker than its Lewis acid binding energy by ~0.3 eV. Furthermore, ammonia was weakly bound at the terminal ZnOH hydroxyl of the Zn-3-OH model, comparable to binding at a terminal silanol for the same model.

Simulated infrared vibrational frequencies for binding of ammonia at Lewis acid sites resulted in two modes for each model in the 1700–1590 cm^{-1} region (Table S15) that could both be assigned to the $\delta_{as}(NH_3)$ mode of NH_3*, consistent with previous DFT calculations.[62] Overall, the vibrational frequency of the $\delta_{as}(NH_3)$ mode for NH_3* follows the order Zn-4c ~ Zn-3-OH > Zn-catalyst.

3.10. CH_3CH_2OH-TPSR-MS. Fundamental kinetic phenomena of the supported ZnO/SiO_2 catalysts were chemically probed with CH_3CH_2OH-TPSR-MS. For supported 2% ZnO/SiO_2-IWI with a 420 °C oxidative pretreatment (Figure 4A), both acetaldehyde and H_2 evolve in two peaks according to deconvolution analyses, with the acetaldehyde peak temperatures (Table S16) lower than the corresponding H_2 peak temperatures (Table S17). The difference in peak temperatures indicates that acetaldehyde and H_2 desorption do not share the same elementary step, i.e., that H* recombination is differentiated from CH_3CHO* desorption. However, both acetaldehyde and H_2 evolution begin at approximately the same temperature (~175 °C in Figure 4A), suggesting they derive from a common surface intermediate. Such findings are consistent with observations by Ohira et al. where acetaldehyde and H_2 coevolved during flowing ethanol temperature-programmed reaction over supported ZnO/SiO_2.[9] Neither acetaldehyde nor H_2 production is observed for the SiO_2 support (Figure S27A), but comparable acetaldehyde and H_2 production are observed for the ZnO/SiO_2-IWI and 3.7% ZnO/SiO_2-SEA catalysts with a 420 °C oxidative pretreatment (Figure S27B–E). Indeed, deconvolution analyses show that very similar acetaldehyde yields are obtained for all the supported ZnO_x/SiO_2 catalysts with oxidative pretreatment (Table 1), where the T_{p1} yield constitutes <0.02 mol CH_3CHO (mol Zn)$^{-1}$ and the total (T_{p1} + T_{p2}) yield constitutes <0.05 mol CH_3CHO (mol Zn)$^{-1}$.

https://doi.org/10.1021/acscatal.5c03430
ACS Catal. 2025, 15, 17225–17240

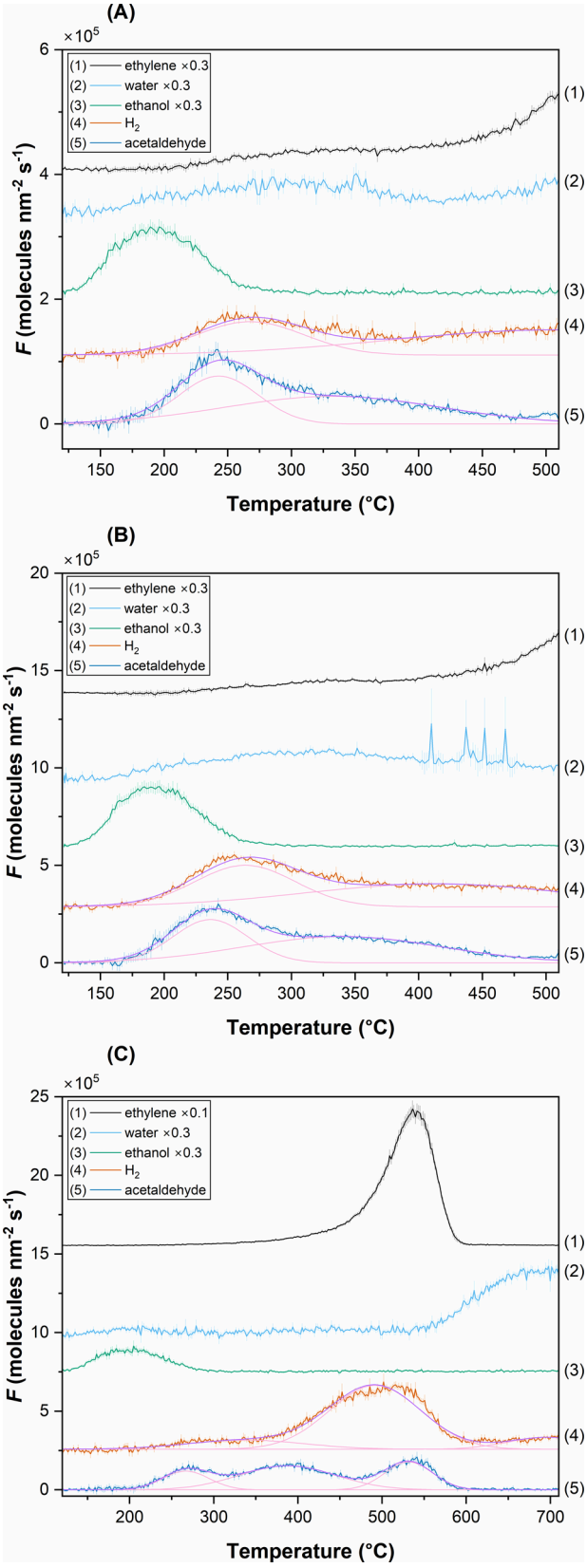

Figure 4. CH_3CH_2OH-TPSR-MS thermograms for 2% ZnO/SiO_2-IWI with (A) 420 °C oxidation pretreatment, (B) 520 °C oxidation pretreatment, and (C) ethanol steady-state reaction pretreatment. The thermograms include (1) ethylene × 0.3 (×0.1 in (C)), (2) water × 0.3, (3) ethanol × 0.3, (4) H_2, and (5) acetaldehyde. Thermograms are vertically offset for clarity. Gaussian deconvolutions are shown in pink with cumulative fits in purple.

The similar results for all the supported ZnO_x/SiO_2 catalysts indicate that only a small fraction of the surface ZnO_x sites are active during CH_3CH_2OH-TPSR-MS. Average CH_3CHO:H_2 yield ratios (Table 1 and Table S18) for T_{p1} and T_{p2} are both 1.2 ± 0.1, respectively, indicating reasonably accurate quantification according to the ethanol dehydrogenation reaction stoichiometry. These quantitative yields also indicate that acetaldehyde evolving with T_{p2} does not arise from readsorption of acetaldehyde, but rather from a second active site. The acetaldehyde and H_2 yields were invariant with respect to ethanol adsorption temperature over the supported 5% ZnO/SiO_2-IWI catalyst (Figure S33B,C), indicating that all surface ZnO_x active sites were titrated at the ethanol feed partial pressure of 1.6 kPa. In summary, only a minor fraction of the surface ZnO_x sites on SiO_2 present at the lowest loading constitute active sites and the additional surface ZnO_x sites are inactive and spectator species.

Molecular ethanol desorbs with a T_p of ∼190 °C (Figure 4 and Figure S27). Varying the temperature of ethanol adsorption over the 5% ZnO/SiO_2-IWI catalyst (Figure S33A) showed that the ethanol desorption T_p increases with decreasing coverage and that the trailing edge of the molecular ethanol thermogram coincided. These characteristics, together with a desorption curve that is symmetrical with respect to temperature, suggest that the surface reaction to yield molecular ethanol is second-order,[64] although heterogeneous sites present on the amorphous silica support could also be responsible. Second-order desorption would be consistent with the reaction between neighboring surface ethoxy species and silanol species[65] that arose from the opening of siloxane bridges upon adsorption, as proposed by Luts and Katz.[21] Alternatively, the disproportionation reaction between adjacent surface ethoxy species may yield molecular ethanol and acetaldehyde.[66] However, no acetaldehyde was observed to desorb from the SiO_2 support (Table 1), so this possibility is not considered further. The CH_3CH_2OH-TPSR-MS of the SiO_2 support (Figure S27A) reveals that ethylene desorption arises from surface ethoxy decomposition on the silica surface.[21] Additional observed byproducts include H_2O, 1,3-butadiene, 3-hexen-1-ol, butenes, 1,3-cyclobutadiene, and acetone (Figure 4 and Figure S28 and Table S20). Detailed identification of 3-hexen-1-ol is shown in Figure S34.

Oxidative pretreatment of the supported 2% ZnO/SiO_2-IWI at 520 °C (Figure 4B) resulted in a larger acetaldehyde and H_2 yields for both T_{p1} and T_{p2} compared to the 420 °C oxidative pretreatment (Table 1 and Table S18). This was consistent with results for supported 1% ZnO/SiO_2-IWI and 7% ZnO/SiO_2-IWI (Table 1 and Table S18). Furthermore, the acetaldehyde and H_2 peak temperatures associated with T_{p1} and T_{p2} decreased with 520 °C oxidative pretreatment compared to 420 °C oxidative pretreatment (Tables S16 and S17). Pretreatment with ethanol reaction (Figure 4C and Figure S31) and ramping to higher temperature revealed a third peak (T_{p3}) for both acetaldehyde and H_2. For ethanol reaction pretreatment of supported 2% ZnO/SiO_2-IWI, 7% ZnO/SiO_2-IWI, and 3.7% ZnO/SiO_2-SEA, the acetaldehyde and H_2 T_{p1} yields remained nearly constant when compared to 420 °C oxidative dehydration pretreatment while the T_{p2} yield increased (Table 1 and Table S18). Furthermore, the acetaldehyde and H_2 peak temperature values associated with T_{p1} and T_{p2} increased with ethanol reaction pretreatment compared to 420 °C oxidative pretreatment (Tables S16 and S17). Larger ethylene yield was observed with ethanol reaction

https://doi.org/10.1021/acscatal.5c03430
ACS Catal. 2025, 15, 17225−17240

Table 1. Acetaldehyde Yield during CH_3CH_2OH-TPSR-MS Associated with Different Desorption Peaks Determined by Gaussian Deconvolution[a]

		acetaldehyde yield (10^3 molecules nm^{-2})		
Pretreatment	sample	T_{p1} (229–280 °C)	T_{p2} (320–411 °C)	T_{p3} (534–543 °C)
420 °C oxidative dehydration	SiO_2	0	0	0
	1% ZnO/SiO_2-IWI	3.9 (2)	6.3 (2)	0
	2% ZnO/SiO_2-IWI	3.4 (2)	5.5 (2)	0
	5% ZnO/SiO_2-IWI	4.3 (2)	4.7 (2)	0
	7% ZnO/SiO_2-IWI	5.5 (3)	6.4 (3)	0
	3.7% ZnO/SiO_2-SEA	15.3(6)	25.4 (8)	0
520 °C oxidative dehydration	1% ZnO/SiO_2-IWI	8.0 (4)	12.3 (4)	0
	2% ZnO/SiO_2-IWI	9.7 (4)	15.4 (4)	0
	7% ZnO/SiO_2-IWI	10.7 (4)	11.2 (4)	0
ethanol reaction	2% ZnO/SiO_2-IWI	4.9 (2)	12.6 (2)	7.4 (1)
	7% ZnO/SiO_2-IWI	5.7 (2)	10.2 (2)	5.04 (8)
	3.7% ZnO/SiO_2-SEA	9.6 (3)	26.3 (4)	8.9 (2)

[a]The number in parentheses indicates the standard deviation in the least significant digit (e.g., 9.1 (4) ≡ 9.1 ± 0.4).

pretreatment, consistent with ethoxylation of free silanols at elevated temperatures.[21] Altogether, it is shown that the number of surface ZnO_x active sites and their intrinsic kinetics for ethanol dehydrogenation were modified depending on the pretreatment conditions.

It was determined that the TPSR experiments could be modeled as a differential reactor without readsorption (Section S2.6.1). Therefore, the enthalpic barrier (E_a) for acetaldehyde evolution was determined by the Redhead analysis method (Table S18), assuming a first-order reaction step and a kinetic prefactor of $\nu = 10^9$ s^{-1} determined from inversion analysis (Section S2.6.2). The smaller than typical[67] (e.g., 10^{13} s^{-1}) kinetic prefactor is consistent with those experimentally measured for adsorbate dissociation[68] and acetic, propionic, and butyric acid decomposition on single crystal surfaces.[69] The value of the kinetic prefactor might be attributed to the loss of entropy of the reactive intermediates as they coordinate to the surface during the rate-determining transition state.[68,69]

A modest linear correlation was observed between CH_3CHO T_{p1} and T_{p2} (Figure S37), suggesting that a common parameter affects activity at disparate active sites. According to the determined reactor model, interparticle and intraparticle readsorption need not be invoked, ruling out that T_{p2} simply arises from ethanol readsorption and reaction. The nature of the relationship between T_{p1} and T_{p2} is further discussed in Section S3.1.

Furthermore, it was found that the acetaldehyde T_{p1} yield was linearly correlated with the ethanol yield across all ZnO/SiO_2 catalysts and pretreatment conditions (Figure 5). However, ethanol had a much lower T_p than acetaldehyde, indicating that these products do not derive from the same rate-determining step. This quantity of ethanol increased with higher temperature oxidative pretreatment, but not particularly with subsequent ethanol reaction pretreatment. The slope of the linear regression indicates a similar quantity of ZnO_x active sites as labile siloxane bridges. The x-intercept of the linear regression ($(3 \pm 3) \times 10^{-3}$ ethanol molecules nm^{-2}) was lower than the ethanol yield obtained from CH_3CH_2OH-TPSR-MS of the SiO_2 support after 420 °C oxidative pretreatment (Table S20). Again, the determined reactor model rules out that the increased acetaldehyde yield was due to readsorption and reaction of ethanol. The activation energy (E_a) for acetaldehyde production associated with T_{p1} was poorly correlated with the ethanol yield (R^2 = 0.01) and the acetaldehyde yield associated with T_{p1} (R^2 = 0.01). The implications of these findings are further discussed in Section 4.6.

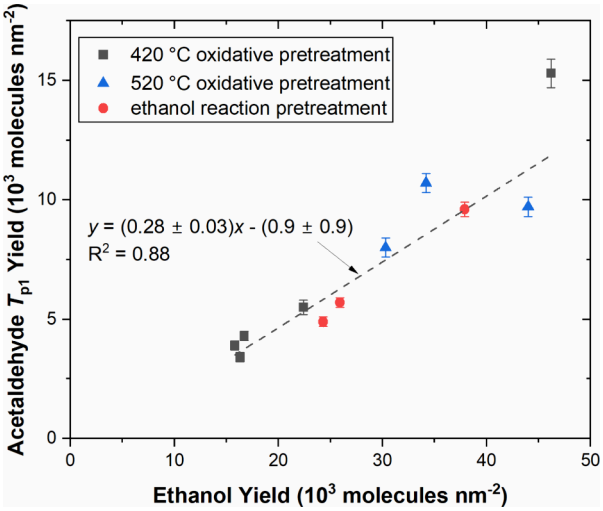

Figure 5. Acetaldehyde T_{p1} yield as a function of ethanol yield for ZnO/SiO_2 catalysts pretreated with 420 °C oxidation (square), 520 °C oxidation (triangle), and ethanol reaction (circle). Dashed black line indicates linear regression fit of all points.

3.11. Catalyst Testing. Turnover frequencies (TOFs) for ethanol dehydrogenation by the supported 1% ZnO/SiO_2-IWI catalyst are shown in Figure 6. The apparent activation energy for ethanol dehydrogenation was determined to be 93 ± 7 kJ mol^{-1} while the selectivity to acetaldehyde was 100% (Table S28).

4. DISCUSSION

4.1. Anchoring Sites for ZnO_x on SiO_2. The supported ZnO_x phase predominantly anchors to form 4-/5-/6-membered zinc-silicate rings by consuming isolated silanols (*in situ* DRIFTS and UV Raman). A portion of ZnO_x sites also anchored at 3-membered siloxane rings (3MR) for supported 2% ZnO/SiO_2-IWI. Schweitzer et al. previously proposed that Zn anchored at 3MR form a more stable 4-membered zinc-silicate ring (three silicon atoms and one zinc atom), consistent with their findings from DFT calculations.[17] Anchoring at 3MR, however, was not indicated for higher

https://doi.org/10.1021/acscatal.5c03430
ACS Catal. 2025, 15, 17225−17240

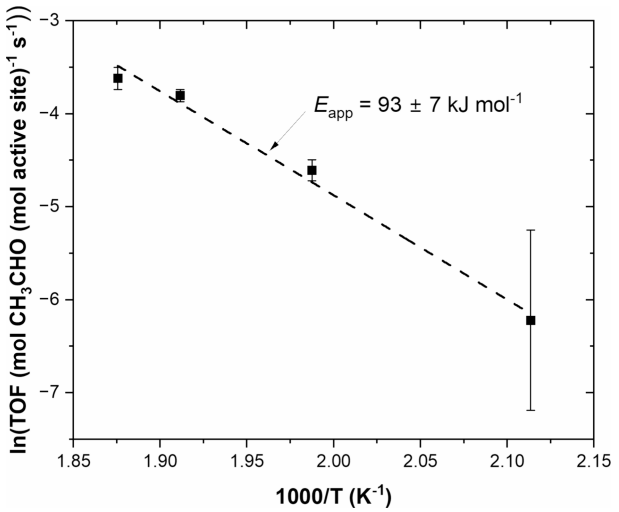

Figure 6. Turnover frequencies for ethanol dehydrogenation to acetaldehyde by 1% ZnO/SiO_2-IWI as a function of inverse temperature (3.1 kPa CH_3CH_2OH, 200−260 °C). Line represents fit to the Arrhenius equation. The number of active sites was determined from total CH_3CHO yield during CH_3CH_2OH-TPSR-MS with 520 °C oxidative pretreatment.

surface ZnO_x densities (supported 7% ZnO/SiO_2-IWI and 3.7% ZnO/SiO_2-SEA). Together, these results suggest that the synthetic methods applied herein (zinc acetate IWI and SEA with prolonged exposure of SiO_2 to basic conditions) did not consistently anchor ZnO_x at 3MR for higher ZnO_x loadings. It is concluded that the detailed synthesis methodology has a profound impact on the anchoring sites of ZnO_x on SiO_2.

4.2. Molecular Structures of Surface ZnO_x Sites on SiO_2. *4.2.1. Dehydrated Conditions.* In contrast to previous literature that reported 3D Zn-containing phases,[12,13] the dehydrated supported ZnO/SiO_2 catalysts synthesized in this study exclusively contained two-dimensional dispersion (*in situ* UV−vis and HS-LEIS).

From *in situ* UV−vis, HS-LEIS, DRIFTS, Raman, XANES, and EXAFS, the molecular structure for the majority of the surface ZnO_x sites for ZnO/SiO_2-IWI and ZnO/SiO_2-SEA catalysts examined herein is proposed in Scheme 2A (type I site, $(\equiv SiO)_2ZnO_2Si=$). Although obtained under *ex situ* conditions, ^{29}Si NMR studies of ZnO_x-SiO_2 by Kunkel et al. also showed an increase in silicon atoms with both one and two nonbridging oxygens (Q^3 and Q^2 species, respectively) compared to the SiO_2 support.[16] With increased surface density of type I sites, a greater diversity of surface ZnO_x local structures was observed as indicated by *in situ* DR UV−vis spectroscopy. Zn_1O_4 sites are estimated to constitute 0.9 ± 0.3 mol Zn_1O_4 (mol Zn)$^{-1}$ for supported ZnO/SiO_2-IWI and ZnO/SiO_2-SEA catalysts based on the oxygen first shell coordination determined by *in situ* EXAFS fitting (Tables S11−S13), assuming that other sites possess ZnO_3 coordination, *vide infra*.

Scheme 2. (A) Proposed Molecular Structure for Type I Sites that Constitute the Majority of Surface ZnO_x Sites Present for Supported ZnO/SiO_2-IWI and ZnO/SiO_2-SEA Catalysts and (B) Proposed Molecular Structure of Minority Type II Sites[a]

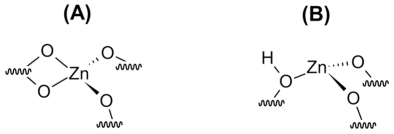

[a]Wavy lines indicate silicon atoms of the silica support

In situ INS suggested and DRIFTS-MS-NH_3-TPD confirmed an additional isolated surface ZnO_x site (type II sites) that possesses a bridging $Zn(OH)^+Si$ hydroxyl (Scheme 2B). Type II sites would be consistent with the Zn_1O_3 molecular structure proposed by Schweitzer et al. containing a bridging hydroxyl.[17]

In contrast to the predominance of surface Zn_1O_3 sites after dehydration treatments observed by Schweitzer et al.[17] (450 °C) and Kunkel et al. (600 °C),[16] in the present study, the predominance of surface Zn_1O_4 sites (type I) is observed. The theoretical literature indicates that temperature (and, thus, entropy) critically determines the relative thermodynamic stability of isolated silica-supported ZnO_x sites. Using DFT calculations, Siodla et al. found that surface ZnO_4 sites were more enthalpically favored than surface ZnO_3 or ZnO_2 sites.[61] Das et al. found that surface ZnO_3 sites were more favored than surface ZnO_4 sites at 550 °C in terms of Gibbs free energy for all siloxane ring sizes examined, while surface ZnO_4 sites (including the oxygen of coordinating water and/or hydroxyls) were favored at 25 °C.[41] Liu et al. also modeled a ZnO_4 site by DFT, albeit with a bridging Zn(OH)Si hydroxyl,[70] different from the type I $(\equiv SiO)_2ZnO_2Si=$ site proposed herein. We propose that the ionic $O_2Si=$ moiety stabilizes ZnO_4 sites to a greater extent than the surface diffusion barrier for Zn cations, which might otherwise access 3MR sites and form surface ZnO_3 sites at elevated temperature. Furthermore, it is suggested that an insufficient entropic driving force to convert ZnO_4 sites into ZnO_3 sites was provided at 400 °C.

4.2.2. Ethanol Dehydrogenation Conditions. *In situ* EXAFS (Section 3.7) indicated minimal changes to the local coordination environment of the dominant surface ZnO_x sites on SiO_2 ($(\equiv SiO)_2ZnO_2Si=$), with the best fits under dehydrated conditions within error of those under reaction conditions. Unfortunately, the signal averaging aspect of XAS (EXAFS/XANES) prevents determining details of minority species such as surface $Zn(OH)^+Si$ Brønsted acid sites.

4.3. Surface Acidity of Supported ZnO_x/SiO_2 Catalysts. Minority weaker Lewis acid−Brønsted acid pair sites were indicated by *in situ* DRIFTS-MS-NH_3-TPD, with similar adsorption enthalpies for each site in the pair. Such pair sites are consistent with the molecular structure of type II sites, with a Lewis acidic Zn cation and Brønsted acidic $Zn(OH)^+Si$ hydroxyl. DFT calculations (model Zn catalyst) corroborated the similar binding energies of NH_3* and (NH_4^+)* adsorbed at type II sites. While type I sites were linearly correlated with Zn loading according to *in situ* Raman and was consistent with characterization by *in situ* EXAFS, *in situ* DRIFTS-MS-NH_3-TPD indicated much lower surface densities of Lewis and Brønsted acid sites. Therefore, it may be concluded that type I sites do not (or minimally) possess Lewis nor Brønsted acidic character. This finding is consistent with DFT calculations of NH_3 adsorption on a Zn_1O_4 site with a Q^2 silicon ligand (model Zn-4c). The presence of a stronger Lewis acid site (type β) determined from *in situ* DRIFTS-MS-NH_3-TPD indicates a third isolated ZnO_x site identified as type III. Several candidate molecular structures for type III sites have been reported in the theoretical literature, such as $(\equiv SiO)_2Zn$ structures.[61]

https://doi.org/10.1021/acscatal.5c03430
ACS Catal. 2025, 15, 17225−17240

4.4. Active Sites for Ethanol Dehydrogenation by Supported ZnO_x/SiO_2 Catalysts. The active sites for ethanol dehydrogenation constitute only a small fraction of the isolated surface ZnO_x sites for the supported ZnO/SiO_2-IWI and ZnO/SiO_2-SEA catalysts (CH_3CH_2OH-TPSR-MS results showed that <0.02 mol CH_3CHO (mol Zn)$^{-1}$ evolved for T_{p1} and <0.03 mol CH_3CHO (mol Zn)$^{-1}$ for T_{p2}). The CH_3CHO yield for T_{p1} and T_{p2} were linearly correlated with the total number of surface Lewis acid sites (Figure S38A) and also surface Brønsted acid sites (Figure S38B), but with slopes much less than unity. These results indicate that a subset of surface ZnO_x sites possessing both Lewis and Brønsted acid sites (i.e., subset of type II sites) constitute the active site for ethanol dehydrogenation. It is suggested that the local strain experienced by site II on the amorphous silica support influenced their relative activity (whether associated with the more kinetically relevant T_{p1} or the less active T_{p2}).[71,72] By contrast, no correlation is observed between acetaldehyde yield and Q^2 species associated with type I sites (Figure S38C). It is, therefore, concluded that site I is inactive for ethanol dehydrogenation. *In situ* XANES corroborates these findings, with a smaller fraction of surface ZnO_x sites coordinated by adsorbates under reaction conditions (Table S8) for supported 7% ZnO/SiO_2-IWI vs. 2% ZnO/SiO_2-IWI, confirming a greater fraction of inactive surface ZnO_4 sites for 7% ZnO/SiO_2-IWI. Furthermore, the total acetaldehyde yield from CH_3CH_2OH-TPSR-MS after ethanol reaction for 2% ZnO/SiO_2-IWI (0.0535 ± 0.0006 mol CH_3CHO (mol Zn)$^{-1}$)), and 7% ZnO/SiO_2-IWI (0.0129 ± 0.0002 mol CH_3CHO (mol Zn)$^{-1}$)), respectively, is close to the fraction of ZnO_x sites coordinated by adsorbates as estimated by *in situ* XANES, suggesting that only active surface ZnO_x sites coordinate reaction intermediates among all surface ZnO_x sites on SiO_2.

Considering the relationships between surface acidity and ZnO_x surface density together with active site quantification, we estimate $(\equiv SiO)_2ZnO_2Si=$ sites, $Zn(OH)^+Si$ Lewis acid–Brønsted acid pair sites, and type III sites comprise approximately ≥77, ≤5, and 18% of all surface ZnO_x sites, respectively, for the catalysts investigated herein.

Considering the work of Schweitzer et al.,[17] our results suggest that SEA synthesis, with minimized exposure of the silica support to basic solutions, will maximize the number of Zn_1O_3 sites active for the ethanol dehydrogenation. Furthermore, pretreatments under elevated temperature (and vacuum) that dehydroxylate the silica support[16,41,73] will promote the conversion of inactive ZnO_x sites into those active for ethanol dehydrogenation.

An inverse linear correlation is found between CH_3CH_2OH-TPSR-MS acetaldehyde yield and the Zn^{2+} LMCT fwhm from DR UV–vis (Figure S38D). Together, these results suggest that a decreasing heterogeneity of surface ZnO_x sites on SiO_2 may be correlated with an increasing fraction of active sites among all surface ZnO_x sites. Indeed, supported ZnO/SiO_2 catalysts prepared from atomic layer deposition (ALD) exhibited a narrower and blue-shifted Zn^{2+} LMCT band compared to that prepared from SEA under *ex situ* conditions.[43] It was shown elsewhere that the SEA catalyst had ZnO_4 coordination under *ex situ* conditions.[17] While this difference in LMCT bands was ascribed to higher dispersion for the ALD catalyst,[43] it was previously demonstrated that the SEA catalyst possessed isolated surface Zn_1O_3 sites under dehydrated conditions[17] (and not ZnO_x sites with larger domain size). Therefore, it is proposed that surface ZnO_x sites on SiO_2 with different local geometry may exhibit slightly different Zn^{2+} LMCT band peak positions.

4.5. Intrinsic Kinetics for Ethanol Dehydrogenation by Silica-Supported Surface ZnO_x Active Sites. From steady-state kinetic studies of ethanol dehydrogenation over Zn-deAlBEA, Qi et al. found that the intrinsic activation energy for ethanol dehydrogenation was 141 ± 1 kJ/mol.[10] From DFT and coupled cluster calculations, Jeevapong et al. found that the Gibbs free energy barrier for ethoxy α-C–H cleavage over Zn-deAlBEA was 144 kJ/mol.[74] These barriers are larger than those measured herein for ethanol dehydrogenation associated with T_{p1} (Table S19). The activation enthalpy for acetaldehyde evolution determined herein was found to be inversely correlated with the Zn^{2+} LMCT fwhm from *in situ* DR UV–vis associated with greater surface site heterogeneity (Figure S39). These results indicate that as surface ZnO_x accessed more diverse local structures on the silica support, greater intrinsic reactivity was achieved. Since the Zn^{2+} LMCT fwhm was directly correlated with ZnO loading for ZnO/SiO_2-IWI (Table S5), this suggests that the limited availability of anchoring sites at higher loadings forced ZnO_x species to adopt more reactive configurations. By contrast, the silica surface for the ZnO/SiO_2-SEA catalyst was altered prior to Zn uptake during synthesis. Active sites may possess a distribution of intrinsic kinetics, especially for surface MO_x sites supported on amorphous supports where each metal atom resides in a unique ligand environment.[72] This increased reactivity is proposed to be related to the local strain experienced by these surface ZnO_x active sites.[71] Such strain would be dictated by the size of the zinc-siloxane ring(s) formed by the anchoring of ZnO_x on the silica support.[41] Thus, the inactive $(\equiv SiO)_2ZnO_2Si=$ plays an indirect role in ethanol dehydrogenation catalysis by titrating anchoring sites on the silica support that are less strained.

During steady-state kinetics at 260 °C, the TOF for 1% ZnO/SiO_2-IWI was comparable to the site time yield (STY) for Zn-deAlBEA reported by Qi et al. (Table S28).[10] However, the apparent activation energy determined herein for 1% ZnO/SiO_2-IWI was lower than that determined for Zn-deAlBEA and closer to that determined for ZnO/SiO_2 by Ohira et al.[9] (Table S29). Together with the similar intrinsic activation energy determined from CH_3CH_2OH-TPSR-MS, this suggests that ethanol adsorbates were nearly saturated on silica-supported ZnO_x sites, like ZnO_x sites within dealuminated BEA hosts at the applied conditions. Such findings are consistent with LCF analysis of *in situ* XANES during ethanol reaction. This adsorption regime follows from the rate expression developed by Qi et al. for ethanol dehydrogenation over Zn-deAlBEA assuming dissociative adsorption of ethanol and rate-limiting α-H abstraction.[10]

4.6. Variation in the Number of ZnO_x Active Sites under Different Pretreatment Conditions and the Kinetic Relationship between Active Sites. We found that the higher pretreatment temperature was associated with both larger acetaldehyde and ethanol yields during TPSR (Table 1 and Table S20). According to model proposed by Luts and Katz,[21] the ethanol yield provides a quantitative measure of the number of labile siloxane bridges formed during the pretreatment step. Luts and Katz proposed that geminal silanols provided the platform for physisorbed ethanol that subsequently opened siloxane bridges.[21] However, Zhuravlev found that the population of total silanols and geminal silanols decreased with increasing temperature.[75] Together, this

https://doi.org/10.1021/acscatal.5c03430
ACS Catal. 2025, 15, 17225–17240

indicates that the increased number of ZnO_x active sites and labile siloxane bridges with increased pretreatment temperature were not associated with geminal silanols. Rather, it appears that the increased surface density of both sites is associated with the increased thermal energy necessary for dehydroxylation processes.[73] Earlier experimental[17] and theoretical[41] findings indicated that certain ZnO_4 sites converted to ZnO_3 sites *via* the loss of coordinating water upon dehydration. Here, we suggest that the extent of dehydroxylation of the silica surface, as probed by ethanol desorption during TPSR, serves as a proxy for the extent of dehydroxylation or decreased coordination to hemilabile[76] siloxane ligands at ZnO_x surface sites, converting them into active sites for ethanol dehydrogenation.

Alternatively, the quantitatively similar and proportional relationship between T_{p1} acetaldehyde yield and ethanol yield may suggest that a portion of ethanol adsorbed at ZnO_x sites desorbed as intact ethanol in parallel to dehydrogenation during TPSR. Indeed, experimental[10] and theoretical[74] studies found comparable ethanol adsorption enthalpies at ZnO_x sites over Zn-deAlBEA as experimentally determined for ethanol adsorption on silica.[77] However, larger ethanol yield was obtained with lower-temperature ethanol adsorption while acetaldehyde yield did not increase. This indicates that these sites are not necessarily paired. Thus, ethanol is also expected to serve as a good marker of the dehydroxylation of the silica surface.

5. CONCLUSIONS

Multiple isolated surface ZnO_x sites are present on silica-supported zinc oxide catalysts. The surface $(\equiv SiO)_2ZnO_2Si=$ sites constituted most of the dispersed ZnO_x sites but were inactive for ethanol dehydrogenation to acetaldehyde. A minority of dispersed ZnO_x sites possessed exclusively Lewis acidic character, and even fewer sites possessed a Brønsted acidic $Zn(OH)^+Si$ moiety. A subset of isolated surface ZnO_x sites possessing both Lewis and Brønsted acidic character were active for ethanol dehydrogenation. It was found that active sites could be further grouped into two distributions with faster and slower intrinsic kinetics. Greater heterogeneity among all surface ZnO_x sites was associated with lower enthalpic barriers for acetaldehyde production among the most active surface ZnO_x sites. These findings suggested that anchoring inactive surface $(\equiv SiO)_2Zn^{2+}O_2Si$ = sites on the silica support caused a greater number of active surface ZnO_x sites to adopt a more strained configuration that lowered the enthalpic barrier for ethanol dehydrogenation. Pretreatments and catalysts that promoted surface dehydroxylation were also associated with increasing the number of the most active surface ZnO_x sites. This finding suggested that inactive surface ZnO_x were activated for ethanol dehydrogenation catalysis by dehydroxylation and/or decreased coordination to hemilabile siloxane ligands.

■ ASSOCIATED CONTENT

Supporting Information

The Supporting Information is available free of charge at https://pubs.acs.org/doi/10.1021/acscatal.5c03430.

Methods, including for N_2 physisorption, powder X-ray diffraction (XRD), *ex situ* and *in situ* high-sensitivity low energy ion scattering (HS-LEIS) under dehydrated conditions, *in situ* diffuse reflectance infrared Fourier transform spectroscopy (DRIFTS) under dehydrated conditions, *in situ* UV Raman spectroscopy under dehydrated conditions, *in situ* diffuse reflectance (DR) UV−vis spectroscopy under dehydrated conditions, *in situ* inelastic neutron scattering (INS) spectroscopy under dehydrated conditions, *in situ* X-ray absorption spectroscopy (XAS) under dehydrated and reaction conditions, *in situ* diffuse reflectance infrared Fourier transform spectroscopy−mass spectrometry (DRIFTS-MS) during NH_3 temperature-programmed desorption (NH_3-TPD), density function theory (DFT) calculations of NH_3 adsorption, ethanol-temperature-programmed surface reaction-mass spectrometry (CH_3CH_2OH-TPSR-MS), and catalyst testing; results including N_2 physisorption, powder X-ray diffraction, *in situ* DRIFTS including impact of mesh "chair" on DRIFTS spectra, *in situ* X-ray absorption spectroscopy including inspection of the *in situ* EXAFS spectra and wavelet transform (WT) analysis of *in situ* EXAFS spectra, *in situ* DRIFTS-MS NH_3-TPD, CH_3CH_2OH-TPSR-MS including determination of appropriate reactor model and inversion analysis, catalyst testing including assessment of reactor scale phenomena, impact of dilution, achievement of steady-state conditions, and assessment of pellet scale phenomena; discussion including the relationship between intrinsic kinetics of disparate ZnO_x active surface sites; illustration of the mesh "chair" setup, N_2 physisorption, powder XRD, *in situ* and *ex situ* HS-LEIS, *in situ* DRIFTS, *in situ* DRIFTS showing impact of mesh "chair", *in situ* UV Raman, *in situ* DR UV−vis, *in situ* INS, DFT models used to simulate atom-projected INS spectra, atom-projected INS spectra, XANES, linear combination fits of XANES spectra, EXAFS, WT of EXAFS spectra, fits of EXAFS spectra, *in situ* DRIFTS-MS NH_3-TPD, schematics of DFT models of NH_3 adsorption, CH_3CH_2OH-TPSR-MS thermograms with oxidative and ethanol reaction pretreatments for major and minor products, as a function of ethanol adsorption temperature, identification of (*E*)-3-hexen-1-ol product, CH_3CH_2OH-TPSR-MS thermograms as a function of catalyst pellet size fraction and sample mass loading, inversion analysis, activation energy correlation between acetaldehyde associated with T_{p1} and T_{p2}, correlations of acetaldehyde yield with semiquantitative characterization, correlation of enthalpic barrier for acetaldehyde evolution with Zn^{2+} LMCT fwhm from *in situ* DR UV−vis, and reaction rates as a function of time on stream during catalyst testing; XAS processing parameters, N_2 physisorption results, assignments for Raman vibrational modes, DR UV−vis fitting results, atom-projected simulated INS modes, E_0 parameter from XANES, linear combination fitting results from XANES, summary of maxima of the EXAFS WT, EXAFS fitting results, ammonia yield from *in situ* DRIFTS-MS NH_3-TPD, DFT-calculated binding energies of ammonia, DFT-simulated infrared vibrational frequencies of adsorbed ammonia, from CH_3CH_2OH-TPSR-MS: acetaldehyde peak temperatures, molecular hydrogen peak temperatures, molecular hydrogen yield, enthalpic barriers for acetaldehyde evolution, yield of byproducts, for catalyst testing: parameters for the assessment of axial convective diffusion, radial diffusion, impact of catalyst bed dilution,

https://doi.org/10.1021/acscatal.5c03430
ACS Catal. 2025, 15, 17225−17240

internal mass transfer limitations, internal heat transfer limitations, external heat transfer limitations, external mass transfer limitations, acetaldehyde turnover frequency and site time yield, and comparison of apparent activation energies from this work and literature (PDF)

AUTHOR INFORMATION

Corresponding Author

Israel E. Wachs − *Operando Molecular Spectroscopy and Catalysis Laboratory, Department of Chemical & Biomolecular Engineering, Lehigh University, Bethlehem, Pennsylvania 18015, United States;* orcid.org/0000-0001-5282-128X; Email: iew0@lehigh.edu

Authors

Benjamin M. Moskowitz − *Operando Molecular Spectroscopy and Catalysis Laboratory, Department of Chemical & Biomolecular Engineering, Lehigh University, Bethlehem, Pennsylvania 18015, United States;* Present Address: Energy and Environment Directorate, Pacific Northwest National Laboratory, 902 Battelle Boulevard, Richland, Washington 99352, United States; orcid.org/0000-0003-1005-8639

Jisue Moon − *Chemical Sciences Division, Oak Ridge National Laboratory, Oak Ridge, Tennessee 37831, United States*

Yuanyuan Li − *Department of Materials Science and Chemical Engineering, Stony Brook University, Stony Brook, New York 11794, United States;* Present Address: Chemical Sciences Division, Oak Ridge National Laboratory, Oak Ridge, Tennessee 37831, United States

Yongqiang Cheng − *Neutron Scattering Division, Oak Ridge National Laboratory, Oak Ridge, Tennessee 37831, United States;* orcid.org/0000-0002-3263-4812

Luke L. Daemen − *Neutron Scattering Division, Oak Ridge National Laboratory, Oak Ridge, Tennessee 37831, United States*

Lane Lee − *Chemical Sciences Division, Oak Ridge National Laboratory, Oak Ridge, Tennessee 37831, United States*

Victor Fung − *Center for Nanophase Materials Sciences, Oak Ridge National Laboratory, Oak Ridge, Tennessee 37831, United States*

Aditya Savara − *Chemical Sciences Division, Oak Ridge National Laboratory, Oak Ridge, Tennessee 37831, United States;* orcid.org/0000-0002-1937-2571

Anatoly I. Frenkel − *Department of Materials Science and Chemical Engineering, Stony Brook University, Stony Brook, New York 11794, United States; Division of Chemistry, Brookhaven National Laboratory, Upton, New York 11973, United States;* orcid.org/0000-0002-5451-1207

Zili Wu − *Chemical Sciences Division and Center for Nanophase Materials Sciences, Oak Ridge National Laboratory, Oak Ridge, Tennessee 37831, United States;* orcid.org/0000-0002-4468-3240

Complete contact information is available at: https://pubs.acs.org/10.1021/acscatal.5c03430

Author Contributions

The manuscript was written through contributions of all authors. All authors have given approval to the final version of the manuscript.

Notes

The authors declare no competing financial interest.

ACKNOWLEDGMENTS

The authors gratefully acknowledge the assistance of Drs. Sagar Sourav and Nebojsa (Ned) Marinkovic with XAS measurements at Brookhaven National Laboratory. The authors gratefully acknowledge the assistance of Eli Ream for DRIFTS measurement of the SiO_2-NH_4OH sample. The authors gratefully acknowledge Adhika Setiawan and Dr. Srinivas Rangarajan for DFT calculations of NH_3 adsorption. This material is based upon work supported by the National Science Foundation under Grant No. 1605805 and by the U.S. Department of Energy (DOE), Office of Science, Office of Workforce Development for Teachers and Scientists, Office of Science Graduate Student Research (SCGSR) Program. The SCGSR Program is administered by the Oak Ridge Institute for Science and Education for the DOE under contract number DE-SC0014664. J.M., A.S., and Z.W. acknowledge support from the U.S. Department of Energy, Office of Science, Office of Basic Energy Sciences, Chemical Sciences, Geosciences, and Biosciences Division, Catalysis Science program. Work by L.L. was supported by the U.S. Department of Energy, Office of Science, Office of Workforce Development for Teachers and Scientists (WDTS) under the Community College Internships (CCI) Program. A.I.F. acknowledges support of his contribution to XAS data analysis by the US National Science Foundation under award 2452446. This research was conducted in part at the Center for Nanophase Materials Sciences at Oak Ridge National Laboratory, which is a DOE Office of Science User Facility. This research benefited from the use of the VISION beamline (IPTS-16527) at the Spallation Neutron Source, Oak Ridge National Laboratory (ORNL), which is supported by the Scientific User Facilities Division, Office of Basic Energy Sciences, U.S. DOE. This research made use of computing resources through the VirtuES and the ICE-MAN projects, funded by Laboratory Directed Research and Development program and Compute and Data Environment for Science (CADES) at ORNL. This research used beamline 7-BM (QAS) of the National Synchrotron Light Source II, a U.S. DOE Office of Science User Facility operated for the DOE Office of Science by Brookhaven National Laboratory under Contract No. DE-SC0012704. Beamline operations were supported in part by the Synchrotron Catalysis Consortium (US DOE, Office of Basic Energy Sciences, Grant No. DESC0012335).

REFERENCES

(1) Pomalaza, G.; Ponton, P. A.; Capron, M.; Dumeignil, F. Ethanol-to-Butadiene: The Reaction and Its Catalysts. *Catal. Sci. Technol.* **2020**, *10* (15), 4860−4911.

(2) Makshina, E. V.; Dusselier, M.; Janssens, W.; Degrève, J.; Jacobs, P. A.; Sels, B. F. Review of Old Chemistry and New Catalytic Advances in the On-Purpose Synthesis of Butadiene. *Chem. Soc. Rev.* **2014**, *43* (22), 7917−7953.

(3) Sushkevich, V. L.; Ivanova, I. I.; Ordomsky, V. V.; Taarning, E. Design of a Metal-Promoted Oxide Catalyst for the Selective Synthesis of Butadiene from Ethanol. *ChemSusChem* **2014**, *7* (9), 2527−2536.

(4) Chieregato, A.; Velasquez Ochoa, J.; Bandinelli, C.; Fornasari, G.; Cavani, F.; Mella, M. On the Chemistry of Ethanol on Basic Oxides: Revising Mechanisms and Intermediates in the Lebedev and Guerbet Reactions. *ChemSusChem* **2015**, *8* (2), 377−388.

(5) Taifan, W. E.; Bučko, T.; Baltrusaitis, J. Catalytic Conversion of Ethanol to 1,3-Butadiene on MgO: A Comprehensive Mechanism Elucidation Using DFT Calculations. *J. Catal.* **2017**, *346*, 78−91.

(6) Taifan, W. E.; Yan, G. X.; Baltrusaitis, J. Surface Chemistry of MgO/SiO_2 Catalyst during the Ethanol Catalytic Conversion to 1,3-Butadiene: In-Situ DRIFTS and DFT Study. *Catalysis Science & Technology* **2017**, *7* (20), 4648−4668.
(7) Xu, Y.; Liu, Z.; Han, Z.; Zhang, M. Ethanol/Acetaldehyde Conversion into Butadiene over Sol-Gel ZrO2−SiO2 Catalysts Doped with ZnO. *RSC Adv.* **2017**, *7* (12), 7140−7149.
(8) Dai, W.; Zhang, S.; Yu, Z.; Yan, T.; Wu, G.; Guan, N.; Li, L. Zeolite Structural Confinement Effects Enhance One-Pot Catalytic Conversion of Ethanol to Butadiene. *ACS Catal.* **2017**, *7* (5), 3703−3706.
(9) Ohira, M.; Liu, H.; He, D.; Hirata, Y.; Sano, M.; Suzuki, T.; Miyake, T. Catalytic Performance and Reaction Pathways of Cu/SiO_2 and ZnO/SiO_2 for Dehydrogenation of Ethanol to Acetaldehyde. *Journal of the Japan Petroleum Institute* **2018**, *61* (4), 205−212.
(10) Qi, L.; Zhang, Y.; Conrad, M. A.; Russell, C. K.; Miller, J.; Bell, A. T. Ethanol Conversion to Butadiene over Isolated Zinc and Yttrium Sites Grafted onto Dealuminated Beta Zeolite. *J. Am. Chem. Soc.* **2020**, *142* (34), 14674−14687.
(11) Yan, T.; Dai, W.; Wu, G.; Lang, S.; Hunger, M.; Guan, N.; Li, L. Mechanistic Insights into One-Step Catalytic Conversion of Ethanol to Butadiene over Bifunctional Zn−Y/Beta Zeolite. *ACS Catal.* **2018**, *8* (4), 2760−2773.
(12) Larina, O. V.; Kyriienko, P. I.; Balakin, D. Yu.; Vorokhta, M.; Khalakhan, I.; Nychiporuk, Y. M.; Matolín, V.; Soloviev, S. O.; Orlyk, S. M. Effect of ZnO on Acid-Base Properties and Catalytic Performances of $ZnO/ZrO_2−SiO_2$ Catalysts in 1,3-Butadiene Production from Ethanol-Water Mixture. *Catal. Sci. Technol.* **2019**, *9* (15), 3964−3978.
(13) Chouillet, C.; Villain, F.; Kermarec, M.; Lauron-Pernot, H.; Louis, C. Relevance of the Drying Step in the Preparation by Impregnation of Zn/SiO_2 Supported Catalysts. *J. Phys. Chem. B* **2003**, *107* (15), 3565−3575.
(14) Taifan, W. E.; Li, Y.; Baltrus, J. P.; Zhang, L.; Frenkel, A. I.; Baltrusaitis, J. Operando Structure Determination of Cu and Zn on Supported MgO/SiO_2 Catalysts during Ethanol Conversion to 1,3-Butadiene. *ACS Catal.* **2019**, *9* (1), 269−285.
(15) Catillon-Mucherie, S.; Lauron-Pernot, H.; Louis, C. Preparation of Coimpregnated Cu−Zn on Zn-Modified Silica: Influence of the Basicity of the Support and of the Nature of Zinc Species on the Catalyst Properties. *J. Phys. Chem. C* **2010**, *114* (25), 11140−11147.
(16) Kunkel, B.; Seeburg, D.; Kabelitz, A.; Witte, S.; Gutmann, T.; Breitzke, H.; Buntkowsky, G.; Buzanich, A. G.; Wohlrab, S. Highly Productive $V/Zn-SiO_2$ Catalysts for the Selective Oxidation of Methane. *Catal. Today* **2024**, *432*, No. 114643.
(17) Schweitzer, N. M.; Hu, B.; Das, U.; Kim, H.; Greeley, J.; Curtiss, L. A.; Stair, P. C.; Miller, J. T.; Hock, A. S. Propylene Hydrogenation and Propane Dehydrogenation by a Single-Site Zn^{2+} on Silica Catalyst. *ACS Catal.* **2014**, *4* (4), 1091−1098.
(18) Camacho-Bunquin, J.; Aich, P.; Ferrandon, M.; Getsoian, A.; Das, U.; Dogan, F.; Curtiss, L. A.; Miller, J. T.; Marshall, C. L.; Hock, A. S.; Stair, P. C. Single-Site Zinc on Silica Catalysts for Propylene Hydrogenation and Propane Dehydrogenation: Synthesis and Reactivity Evaluation Using an Integrated Atomic Layer Deposition-Catalysis Instrument. *J. Catal.* **2017**, *345*, 170−182.
(19) Cordon, M. J.; Zhang, J.; Purdy, S. C.; Wegener, E. C.; Unocic, K. A.; Allard, L. F.; Zhou, M.; Assary, R. S.; Miller, J. T.; Krause, T. R.; Lin, F.; Wang, H.; Kropf, A. J.; Yang, C.; Liu, D.; Li, Z. Selective Butene Formation in Direct Ethanol-to-C_{3+}-Olefin Valorization over Zn−Y/Beta and Single-Atom Alloy Composite Catalysts Using In Situ-Generated Hydrogen. *ACS Catal.* **2021**, *11*, 7193−7209.
(20) Zhang, J.; Wegener, E. C.; Samad, N. R.; Harris, J. W.; Unocic, K. A.; Allard, L. F.; Purdy, S.; Adhikari, S.; Cordon, M. J.; Miller, J. T.; Krause, T. R.; Cheng, S.; Liu, D.; Li, M.; Jiang, X.; Wu, Z.; Li, Z. Isolated Metal Sites in Cu−Zn−Y/Beta for Direct and Selective Butene-Rich C_{3+} Olefin Formation from Ethanol. *ACS Catal.* **2021**, *11*, 9885−9897.
(21) Luts, T.; Katz, A. Chemisorption and Dehydration of Ethanol on Silica: Effect of Temperature on Selectivity. *Top Catal* **2012**, *55* (1−2), 84−92.
(22) Iler, R. K. *The Colloid Chemistry of Silica and Silicates*; Cornell University Press: Ithaca, N.Y., London, 1955.
(23) Busca, G. Catalytic Materials Based on Silica and Alumina: Structural Features and Generation of Surface Acidity. *Prog. Mater. Sci.* **2019**, *104*, 215−249.
(24) Gallas, J.-P.; Goupil, J.-M.; Vimont, A.; Lavalley, J.-C.; Gil, B.; Gilson, J.-P.; Miserque, O. Quantification of Water and Silanol Species on Various Silicas by Coupling IR Spectroscopy and In-Situ Thermogravimetry. *Langmuir* **2009**, *25* (10), 5825−5834.
(25) Almeida, R. M.; Guiton, T. A.; Pantano, C. G. Characterization of Silica Gels by Infrared Reflection Spectroscopy. *J. Non-Cryst. Solids* **1990**, *121* (1), 193−197.
(26) Ma, J. G.; Liu, Y. C.; Xu, C. S.; Liu, Y. X.; Shao, C. L.; Xu, H. Y.; Zhang, J. Y.; Lu, Y. M.; Shen, D. Z.; Fan, X. W. Preparation and Characterization of ZnO Particles Embedded in SiO_2 Matrix by Reactive Magnetron Sputtering. *J. Appl. Phys.* **2005**, *97* (10), 103509.
(27) Su, K.; Tilley, T. D.; Sailor, M. J. Molecular and Polymer Precursor Routes to Manganese-Doped Zinc Orthosilicate Phosphors. *J. Am. Chem. Soc.* **1996**, *118* (14), 3459−3468.
(28) Zotov, N.; Ebbsjö, I.; Timpel, D.; Keppler, H. Calculation of Raman Spectra and Vibrational Properties of Silicate Glasses: Comparison between $Na_2Si_4O_9$ and SiO_2 Glasses. *Phys. Rev. B* **1999**, *60* (9), 6383−6397.
(29) Halasz, I.; Kierys, A.; Goworek, J.; Liu, H.; Patterson, R. E. ^{29}Si NMR and Raman Glimpses into the Molecular Structures of Acid and Base Set Silica Gels Obtained from TEOS and Na-Silicate. *J. Phys. Chem. C* **2011**, *115* (50), 24788−24799.
(30) Nelson, C.; Furukawa, T.; White, W. B. Transition Metal Ions in Glasses: Network Modifiers or Quasi-Molecular Complexes? *Mater. Res. Bull.* **1983**, *18* (8), 959−966.
(31) Greaves, G. N.; Fontaine, A.; Lagarde, P.; Raoux, D.; Gurman, S. J. Local Structure of Silicate Glasses. *Nature* **1981**, *293* (5834), 611−616.
(32) Martynowycz, M. W.; Hu, B.; Kuzmenko, I.; Bu, W.; Hock, A.; Gidalevitz, D. Monomolecular Siloxane Film as a Model of Single Site Catalysts. *J. Am. Chem. Soc.* **2016**, *138* (38), 12432−12439.
(33) Rajalakshmi, M.; Arora, A. K.; Bendre, B. S.; Mahamuni, S. Optical Phonon Confinement in Zinc Oxide Nanoparticles. *J. Appl. Phys.* **2000**, *87* (5), 2445−2448.
(34) Scott, J. F. uv Resonant Raman Scattering in ZnO. *Phys. Rev. B* **1970**, *2* (4), 1209−1211.
(35) Frost, R. L.; Bouzaid, J. M.; Jagannadha Reddy, B. Vibrational Spectroscopy of the Sorosilicate Mineral Hemimorphite $Zn_4(OH)_2Si_2O_7·H2O$. *Polyhedron* **2007**, *26* (12), 2405−2412.
(36) Chandra Babu, B.; Rao, B. V.; Ravi, M.; Babu, S. Structural, Microstructural, Optical, and Dielectric Properties of Mn^{2+}: Willemite Zn_2SiO_4 Nanocomposites Obtained by a Sol-Gel Method. *J. Mol. Struct.* **2017**, *1127*, 6−14.
(37) Leinenweber, K.; Navrotsky, A.; McMillan, P.; Ito, E. Transition Enthalpies and Entropies of High Pressure Zinc Metasilicates and Zinc Metagermanates. *Phys. Chem. Minerals* **1989**, *16* (8), 799−808.
(38) Galeener, F. L.; Geissberger, A. E. Vibrational Dynamics in ^{30}Si-Substituted Vitreous SiO_2. *Phys. Rev. B* **1983**, *27* (10), 6199−6204.
(39) Humbert, B.; Burneau, A.; Gallas, J. P.; Lavalley, J. C. Origin of the Raman Bands, D_1 and D_2, in High Surface Area and Vitreous Silicas. *J. Non-Cryst. Solids* **1992**, *143*, 75−83.
(40) Chligui, M.; Guimbretiere, G.; Canizares, A.; Matzen, G.; Vaills, Y.; Simon, P. *New Features in the Raman Spectrum of Silica: Key-Points in the Improvement on Structure Knowledge*, **2010**. https://hal.archives-ouvertes.fr/hal-00520823 (accessed 2019−03−01).
(41) Das, U.; Zhang, G.; Hu, B.; Hock, A. S.; Redfern, P. C.; Miller, J. T.; Curtiss, L. A. Effect of Siloxane Ring Strain and Cation Charge Density on the Formation of Coordinately Unsaturated Metal Sites on Silica: Insights from Density Functional Theory (DFT) Studies. *ACS Catal.* **2015**, *5* (12), 7177−7185.

(42) Skuja, L. Optical Properties of Defects in Silica. In *Defects in SiO2 and Related Dielectrics: Science and Technology*; Pacchioni, G.; Skuja, L.; Griscom, D. L. Eds.; Springer Netherlands: Dordrecht, 2000; pp 73−116. .
(43) Camacho-Bunquin, J.; Ferrandon, M.; Sohn, H.; Yang, D.; Liu, C.; Ignacio-de Leon, P. A.; Perras, F. A.; Pruski, M.; Stair, P. C.; Delferro, M. Chemoselective Hydrogenation with Supported Organoplatinum(IV) Catalyst on Zn(II)-Modified Silica. *J. Am. Chem. Soc.* **2018**, *140* (11), 3940−3951.
(44) Schwarting, M.; Siol, S.; Talley, K.; Zakutayev, A.; Phillips, C. Automated Algorithms for Band Gap Analysis from Optical Absorption Spectra. *Materials Discovery* **2017**, *10*, 43−52.
(45) Yoshida, H.; Shimizu, T.; Murata, C.; Hattori, T. Highly Dispersed Zinc Oxide Species on Silica as Active Sites for Photoepoxidation of Propene by Molecular Oxygen. *J. Catal.* **2003**, *220* (1), 226−232.
(46) Krzywinski, M.; Altman, N. Error Bars. *Nat. Methods* **2013**, *10* (10), 921−922.
(47) Bharti, D. K.; Verma, K.; Srivastava, A. K.; Gupta, M. K. The Effect of Co-Doping on Dielectric Properties and Bandgap of Zinc Silicate Nanowires. *J. Appl. Phys.* **2020**, *127* (8), No. 085104.
(48) Samsudin, N. F.; Matori, K. A.; Liew, J. Y. C.; Wing Fen, Y.; Mohd Zaid, M. H.; Nadakkavil Alassan, Z. Investigation on Structural and Optical Properties of Willemite Doped Mn^{2+} Based Glass-Ceramics Prepared by Conventional Solid-State Method. *Journal of Spectroscopy* **2015**, *2015*, 1−7.
(49) Li, J.-J.; Zhu, B.-L.; Wang, G.-C.; Liu, Z.-F.; Huang, W.-P.; Zhang, S.-M. Role of Hydroxyl Groups in Low-Temperature CO Catalytic Oxidation over $Zn_4Si_2O_7(OH)_2$ Nanowire-Supported Gold Nanoparticles. *J. Phys. Chem. C* **2018**, *122* (44), 25456−25466.
(50) Rohatgi, A. *WebPlotDigitizer*. https://automeris.io/WebPlotDigitizer (accessed 2020−04−22).
(51) Ross-Medgaarden, E. I.; Wachs, I. E. Structural Determination of Bulk and Surface Tungsten Oxides with UV−vis Diffuse Reflectance Spectroscopy and Raman Spectroscopy. *J. Phys. Chem. C* **2007**, *111* (41), 15089−15099.
(52) Li, H.; Paolucci, C.; Khurana, I.; Wilcox, L. N.; Göltl, F.; Albarracin-Caballero, J. D.; Shih, A. J.; Ribeiro, F. H.; Gounder, R.; Schneider, W. F. Consequences of Exchange-Site Heterogeneity and Dynamics on the UV-Visible Spectrum of Cu-Exchanged SSZ-13. *Chem. Sci.* **2019**, *10* (8), 2373−2384.
(53) Cheng, Y. Q.; Daemen, L. L.; Kolesnikov, A. I.; Ramirez-Cuesta, A. J. Simulation of Inelastic Neutron Scattering Spectra Using OCLIMAX. *J. Chem. Theory Comput.* **2019**, *15* (3), 1974−1982.
(54) Temelso, B.; Shields, G. C. The Role of Anharmonicity in Hydrogen-Bonded Systems: The Case of Water Clusters. *J. Chem. Theory Comput.* **2011**, *7* (9), 2804−2817.
(55) Nelson, J. XANES Reflects Coordination Change and Underlying Surface Disorder of Zinc Adsorbed to Silica. *J. Synchrotron Rad* **2021**, *28* (4), 1119−1126.
(56) Wang, J.-F.; Wang, K.-X.; Wang, J.-Q.; Li, L.; Jiang, Y.-M.; Guo, X.-X.; Chen, J.-S. Elucidation of the Chemical Environment for Zinc Species in an Electron-Rich Zinc-Incorporated Zeolite. *J. Solid State Chem.* **2013**, *202*, 111−115.
(57) Raine, E.; Clark, A. H.; Smales, G.; Smith, A.; Gianolio, D.; Li, T.; Zheng, J.; Griffith, B. E.; Hyde, T. I.; Feaviour, M.; Collier, P.; Hanna, J. V.; Sankar, G.; Tsang, S. C. E. Synthesis and Characterization of Platinum Nanoparticle Catalysts Capped with Isolated Zinc Species in SBA-15 cChannels: The Wall Effect. *ACS Applied Nano Materials* **2018**, *1* (12), 6603−6612.
(58) Mei, B.; Becerikli, A.; Pougin, A.; Heeskens, D.; Sinev, I.; Grünert, W.; Muhler, M.; Strunk, J. Tuning the Acid/Base and Structural Properties of Titanate-Loaded Mesoporous Silica by Grafting of Zinc Oxide. *J. Phys. Chem. C* **2012**, *116* (27), 14318−14327.
(59) Morra, E.; Berlier, G.; Borfecchia, E.; Bordiga, S.; Beato, P.; Chiesa, M. Electronic and Geometrical Structure of Zn^+ Ions Stabilized in the Porous Structure of Zn-Loaded Zeolite H-ZSM-5: A Multifrequency CW and Pulse EPR Study. *J. Phys. Chem. C* **2017**, *121* (26), 14238−14245.
(60) Lam, E.; Larmier, K.; Wolf, P.; Tada, S.; Safonova, O. V.; Copéret, C. Isolated Zr Surface Sites on Silica Promote Hydrogenation of CO_2 to CH_3OH in Supported Cu Catalysts. *J. Am. Chem. Soc.* **2018**, *140* (33), 10530−10535.
(61) Siodla, T.; Sobczak, I.; Ziolek, M.; Tielens, F. Theoretical and Experimental Insight into Zinc Loading on Mesoporous Silica. *Microporous Mesoporous Mater.* **2018**, *256*, 199−205.
(62) Suganuma, S.; Murakami, Y.; Ohyama, J.; Torikai, T.; Okumura, K.; Katada, N. Assignments of Bending Vibrations of Ammonia Adsorbed on Surfaces of Metal Oxides. *Catal. Lett.* **2015**, *145* (10), 1904−1912.
(63) Civalleri, B.; Garrone, E.; Ugliengo, P. Cagelike Clusters as Models for the Isolated Hydroxyls of Silica: Ab Initio B3-LYP Calculations of the Interaction with Ammonia. *Langmuir* **1999**, *15* (18), 5829−5835.
(64) Falconer, J. L.; Schwarz, J. A. Temperature-Programmed Desorption and Reaction: Applications to Supported Catalysts. *Catalysis Reviews* **1983**, *25* (2), 141−227.
(65) Danielson, T.; Hin, C.; Savara, A. Generalized Adsorption Isotherms for Molecular and Dissociative Adsorption of a Polar Molecular Species on Two Polar Surface Geometries: Perovskite (100) (Pm-3m) and Fluorite (111) (Fm-3m). *J. Chem. Phys.* **2016**, *145* (6), No. 064705.
(66) Chen, B.; Xiong, C.; Jiang, D.; Savara, A. Ethanol Conversion over $La_{0.7}Sr_{0.3}MnO_{3-x}$(100): Autocatalysis, Adjacent O-Vacancies, Disproportionation, and Dehydrogenation. *ACS Catal.* **2020**, *10* (21), 12920−12931.
(67) Savara, A.; Schmidt, C. M.; Geiger, F. M.; Weitz, E. Adsorption Entropies and Enthalpies and Their Implications for Adsorbate Dynamics. *J. Phys. Chem. C* **2009**, *113* (7), 2806−2815.
(68) Campbell, C. T.; Árnadóttir, L.; Sellers, J. R. V. Kinetic Prefactors of Reactions on Solid Surfaces. *Zeitschrift für Physikalische Chemie* **2013**, *227* (11), 1435−1454.
(69) Chang, S. A.; Vermani, V.; Flaherty, D. W. Effects of Phosphorus and Alkyl Substituents on C-H, C−C, and C−O Bond Rupture within Carboxylic Acids on Ru(0001). *Journal of Vacuum Science & Technology A* **2017**, *35* (5), No. 05C309.
(70) Liu, C.; Camacho-Bunquin, J.; Ferrandon, M.; Savara, A.; Sohn, H.; Yang, D.; Kaphan, D. M.; Langeslay, R. R.; Ignacio-de Leon, P. A.; Liu, S.; Das, U.; Yang, B.; Hock, A. S.; Stair, P. C.; Curtiss, L. A.; Delferro, M. Development of Activity-Descriptor Relationships for Supported Metal Ion Hydrogenation Catalysts on Silica. *Polyhedron* **2018**, *152*, 73−83.
(71) Amakawa, K.; Sun, L.; Guo, C.; Hävecker, M.; Kube, P.; Wachs, I. E.; Lwin, S.; Frenkel, A. I.; Patlolla, A.; Hermann, K.; Schlögl, R.; Trunschke, A. How Strain Affects the Reactivity of Surface Metal Oxide Catalysts. *Angew. Chem., Int. Ed.* **2013**, *52* (51), 13553−13557.
(72) Vandervelden, C. A.; Khan, S. A.; Peters, B. Importance Learning Estimator for the Site-Averaged Turnover Frequency of a Disordered Solid Catalyst. *J. Chem. Phys.* **2020**, *153* (24), 244120.
(73) Comas-Vives, A. Amorphous SiO_2 Surface Models: Energetics of the Dehydroxylation Process, Strain, Ab Initio Atomistic Thermodynamics and IR Spectroscopic Signatures. *Phys. Chem. Chem. Phys.* **2016**, *18* (10), 7475−7482.
(74) Jeevapong, W.; Sittiwong, J.; Probst, M.; Boekfa, B.; Wattanakit, C.; Maihom, T.; Limtrakul, J. Density Functional and Coupled Cluster Study on the Conversion of Ethanol to Acetaldehyde on Isolated Zinc Sites Supported on Dealuminated BEA Zeolite. *J. Phys. Chem. C* **2023**, *127* (18), 8473−8481.
(75) Zhuravlev, L. T. The Surface Chemistry of Amorphous Silica. Zhuravlev Model. *Colloids Surf., A* **2000**, *173* (1−3), 1−38.
(76) Fong, A.; Peters, B.; Scott, S. L. One-Electron-Redox Activation of the Reduced Phillips Polymerization Catalyst, via Alkylchromium-(IV) Homolysis: A Computational Assessment. *ACS Catal.* **2016**, *6* (9), 6073−6085.

https://doi.org/10.1021/acscatal.5c03430
ACS Catal. 2025, 15, 17225−17240

(77) Natal-Santiago, M. A.; Dumesic, J. A. Microcalorimetric, FTIR, and DFT Studies of the Adsorption of Methanol, Ethanol, and 2,2,2-Trifluoroethanol on Silica. *J. Catal.* **1998**, *175* (2), 252−268.

https://doi.org/10.1021/acscatal.5c03430
ACS Catal. 2025, 15, 17225−17240